Shang, J., Gui, Y. and Zhao, Z. (2018) Broad-spectrum fracture toughness of an anisotropic sandstone under mixed-mode loading. *Theoretical and Applied Fracture Mechanics*, 96, pp. 556-575. (doi: 10.1016/j.tafmec.2018.07.005).

This is the author's final accepted version.

There may be differences between this version and the published version. You are advised to consult the publisher's version if you wish to cite from it.

http://eprints.gla.ac.uk/226146/

Deposited on: 19 May 2021

Enlighten – Research publications by members of the University of Glasgow
http://eprints.gla.ac.uk

Broad-spectrum fracture toughness of an anisotropic sandstone under mixed-mode loading

J Shang[1], Y Gui[2], Z Zhao[1]

[1]Nanyang Centre for Underground Space,
School of Civil and Environmental Engineering,
Nanyang Technological University, Singapore

[2]School of Engineering, Newcastle University,
Newcastle Upon Tyne, United Kingdom

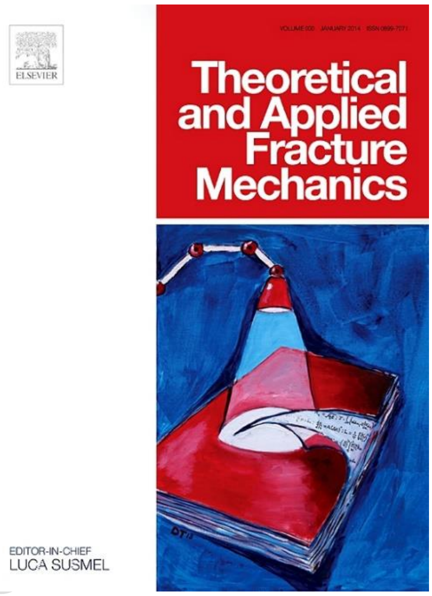

Keywords: Broad-spectrum fracture toughness; Anisotropic rocks; Mixed-mode loading; Discrete Element Method; Fracture criteria

Received date: 11 May 2018
Revised date: 28 June 2018
Accepted date: July 2018

This is a PDF file of an unedited manuscript that has been accepted for publication. The manuscript will undergo copyediting, typesetting, and review of the resulting proof before it is published in its final form. Please note that during the production process errors may be discovered which could affect the content.

ACCEPTED MANU

Abstract

Fracture toughness of anisotropic rocks can vary with many factors such as geological anisotropy, geometrical properties of specimens used in the laboratory (e.g., pre-existing crack properties), and loading conditions. This fact has been widely acknowledged. Yet the variation in fracture toughness remains enigmatic, as there is still lack of a comprehensive study on how those influential factors affect fracture toughness behavior of anisotropic rocks. The present paper shows a broad-spectrum mixed-mode fracture toughness of an anisotropic sandstone from a numerical scheme, which is based on the Discrete Element Method (DEM). In this study, a total of 340 semi-circular bend (SCB) specimens with various geological and geometrical conditions were numerically prepared by systemically varying the orientations

of planar anisotropy (i.e. incipient bedding plane), as well as the magnitudes of the ISRM-suggested geometrical parameters of the SCB specimens (i.e. crack length, crack angle, and span length). The numerical model used in the study was calibrated against a series of laboratory experiments to select proper micro-parameters to reproduce the mechanical characteristics of anisotropic Midgley Grit sandstone (MGS). Additionally, four different fracture criteria, which are based on stress and strain analysis, and the analysis of energy density, were used to predict the mixed-mode fracture behaviour of MGS. Numerical findings from this study were compared with experimental observations (qualitatively) and theoretical predictions (quantitatively). A broad agreement was observed in the comparison study.

1. Introduction

Hydraulic fracturing has been widely used in the unconventional extraction of natural resources, including oil and gas and geothermal energy, for creating flow channels/fractures and enhancing permeability of tight rock formations [1]. The fracturing process will stimulate the flow of natural resources, thereby increasing the volumes that can be recovered. In the fracturing process, a controllable and predictable fracture pattern is of significant importance to the effective recovery of natural resources [2]. However, the fracture pattern can be complex and quite different for different geological settings and stress conditions, especially for fractured reservoirs with anisotropic rocks under mixed-mode loading conditions, which is therefore, difficult to be fully understood. Sustained efforts are therefore, needed for the topic.

Fracture toughness is an important parameter, which is used to characterize the ability of rock to resist fracturing. This parameter is often used as a criterion for predicating fracture initiation which is fundamentally important in understanding the mechanical properties of rocks. Although fracture toughness is often considered as an intrinsic property of a rock material, it still can vary with many factors including geological anisotropy [3, 4], geometrical properties of the laboratory-scale specimens [5-7], temperature [8], and loading conditions [9, 10]. As such, a comprehensive description of the possible variation of fracture toughness arising from those factors is of great

ACCEPTED MANUSCRIPT

importance for a better understanding of the mechanical behaviour of anisotropic rocks, as well as for a proper selection of pressure and viscosity of liquid used for fracturing anisotropic rocks.

For transversely isotropic rocks (a typical form of anisotropy) with bedded layers (i.e., planar anisotropy), the magnitude of fracture toughness differs with respect to the relative orientation between the pre-existing cracks and the transversely isotropic bedding planes. Also, the weakness planes can divert fracture propagation, leading to a complex fracture pattern [11]. For example, Na et al. [4] numerically explored the effects of orientation and length of pre-existing cracks, as well as thickness of bedding planes on the fracture pattern of Mancos shale in Brazilian tests and concluded that geological anisotropy significantly affected fracture patterns and effective fracture toughness (EFT). It was also revealed from that study that the initiation, propagation, and coalescence of fractures within layered geo-materials depended on local heterogeneity.

Previous investigations on the fracture toughness of anisotropic rocks have focused on the mode I loading condition [3, 4, 12] with inadequate attention given to the mixed-mode (i.e., I+II) loading condition which is often seen in nature. Although some attempts exist [13, 14] in the study of the combined effects of geological anisotropy and mixed-mode loading on EFT, a systematic investigation is still needed since only limited scenarios were reported in previous studies. For example, Krishnan et al. [13] reported a series of fracture toughness tests on a layered sandstone under mixed-mode loading, however all tested specimens had their bedding planes perpendicular to the direction of the applied load, without considering cases with bedding planes parallel to the load direction. Roy et al. [14] reported a laboratory investigation on the mixed-mode fracture toughness of a sedimentary rock based on SCB specimens, in which the joint anisotropy (i.e., direct tensile strength) was differentiated based on the work by Shang et al. [15]. In that study, the anisotropic planes within the tested SCB specimens were oriented at a relatively small angle with respect to the loading direction, ignoring the cases with bedding planes perpendicular to the loading direction.

ACCEPTED MANUSCRIPT

As previously mentioned, apart from geological anisotropy and loading conditions, the geometrical properties of specimens used in the laboratory also affect fracture toughness behaviour. It is known that the fracture toughness of a solid material is often measured in the laboratory and there are several suggested specimens for the fracture toughness tests, such as short rod (SR) specimen, semi-circular bend (SCB) specimen and cracked Brazilian disk (CBD) specimen [16, 17]. SCB specimens are popular among others due to the comparatively easier sample machining. A variation of fracture toughness has been observed in previous studies for SCB specimens with different crack lengths. For example, Zhao et al. [18] investigated the effect of crack length on the dynamic fracture toughness of SCB coal specimens and found that the dynamic fracture toughness of the tested coal specimens increased when the crack length was increased from 4 to 10 mm. The effect of span length on fracture toughness may also exist but research on this topic is rare.

The geometrical dimensions of SCB specimens have been recommended by the ISRM standard [17]. However, how the specimen dimensions within the suggested domain affect the magnitude of fracture toughness is not clear. In the laboratory measurement of fracture toughness, as a normal routine, only limited geometrical dimensions (in terms of specimen diameter, thickness, crack length and span length) of SCB specimens are used, which inevitability will lead to an incomplete description of the fracture toughness of targeted materials. Additionally, it has to be accepted that it is tedious and cumbersome for the preparation of SCB specimens in the laboratory when the influential factors described above (i.e., geological, geometrical and loading conditions) are considered simultaneously.

In this paper, a broad-spectrum mixed-mode fracture toughness of an anisotropic SCB sandstone was reported based on a total of 340 Discrete Element Method (DEM) simulations. The broad-spectrum fracture behaviour was achieved by systematically varying the orientation of planar anisotropy, crack length, span length, as well as crack angle in the DEM simulations. The effects of the geological and geometrical factors on fracture toughness were investigated and discussed. The effect of incipiency of planar anisotropy

ACCEPTED MANUSCRIPT

(relative tensile strength) on failure characteristic was also discussed and presented. Numerical findings in the study were compared qualitatively with previous experimental observations, and validated quantitatively against theoretical predictions.

2. Anisotropic Midgley Grit sandstone

In the study, a series of DEM simulations were performed to reproduce the mechanical characteristics of medium-grained Midgley Grit sandstone (MGS), which is produced at the Blachhill Quarry (BQ), United Kingdom (Figs. 1a and 1b). The MGS is from the Carboniferous Midgley Grit Formation (Fig. 1c) and ranges from fine- to very coarse-grained sandstone [15]. The medium-grained MGS targeted in the study presents a transverse isotropy, which can be illustrated by the nicely bedded planes in a core sample (see Fig.1d). A laboratory investigation has been reported by Shang et al. [15] in the measurement of the direct tensile strength of the incipient bedding planes. It was found that the direct tensile strength of those incipient planes varied from 31.3 % to 87.5 % that of intact parent rock (2.08 MPa). The MGS sample used in that study comprised 70 % quartz, 15 % clay, 10 % k-feldspar and ~5 % haematite (Fig. 1e) and the unit weight of the sample is around 22.1 kN/m^3. In this study, bedding planes with a direct tensile strength of 87.5 % that of parent was targeted and modelled.

3. Numerical model setup and calibration

3.1 Numerical model setup

Fig. 2 shows the setup of the numerical model, in which SCB specimens with a single pre-existing crack were used. The setup allows the testing under mode I, mode II, and mixed-mode (I+II) loading conditions by simply varying the crack angles using the same specimen configuration and the same experimental set up [17]. The fracture toughness with different modes can be calculated from Eqs. 1-3 [10, 17]

$$K_{ic} = \frac{P_{\mathrm{f}}\sqrt{\pi a}}{2Rt} Y_i, \quad i = \mathrm{I, II} \tag{1}$$

ACCEPTED MANUSCRIPT

$$K_{\mathrm{E}} = \sqrt{K_{\mathrm{Ic}}^{\ 2} + K_{\mathrm{IIc}}^{\ 2}} \tag{2}$$

$$T = \frac{P_{\mathrm{f}}}{2Rt} T^{*} \tag{3}$$

where: K_{Ic} , K_{IIc} and K_{E} are mode I, mode II and mixed-mode fracture toughness, respectively (mixed-mode fracture toughness is also termed as effective fracture toughness (ETF) in the study.); T is the T-stress in SCB specimens; P_f is the peak load at the time of sample failure; a is the crack length; R denotes the sample radius and t represents the sample thickness. Y_I and Y_{II} are dimensionless geometry factors for mode I and mode II loading conditions, respectively; and T^* also is a geometry factor and values of these factors of SCB specimens are depended on the crack length (a), span length ($2s$) as well as crack angle (β).

The three-dimensional Particle Flow Code which implements the DEM technique was used to construct the SCB specimens. Particles having a radius ranging between 0.8 and 1.2 mm, which follows a uniform distribution, were used and a total of 22666 particles were generated (Fig. 2a). A loading bar (red, Fig. 2) was generated on the top of the SCB specimens and two supporting bars (blue) were created at the bottom with varying spans (i.e., 2s). A constant loading rate (LR) of 0.001 m/s was applied on the loading bar to simulate static equilibrium state. Simulations terminated when the axial load (P) dropped to 70 % of peak load, and the peak load was monitored and used for the calculation of fracture toughness based on Eqs. 1-3. In the construction of the DEM specimens, two different contact models were used to bond the particles (see the close-up view, Fig. 2a). The flat joint contact model (FJCM) was used for bonding the particles of the rock matrix to eliminate the intrinsic drawback of the standard bonded particle model [19, 20] (i.e., unrealistic low compressive-to-tensile strength ratio); while the smooth joint contact model (SJCM) was selected for bonding the particles laying on the opposite side of the bedding planes to eliminate unrealistic dilation arising from the spherical particles [21].

ACCEPTED MANUSCRIPT

In the study, a total of 340 DEM specimens with different geometrical and geological properties were prepared. The specimen radius (*R*) and thickness (*t*) remained constant, which were 50 and 30 mm, respectively (Fig. 2). The crack length (*a*) and span length (2*s*) were varied within the range recommended by ISRM [17] (i.e., $0.4 \le a/R \le 0.6$ and $0.5 \le s/2R \le 0.8$). Specifically, the crack length were 20, 25 and 30 mm, respectively. For specimens with a crack length of 20 mm, a span length of 50 and 55 mm were selected respectively to ensure that all tested specimens having this specific crack length (i.e., 20 mm) can provide a complete mode of fracture toughness (i.e., mode I, mode II and mixed-mode I+II) [22]. Similarly, for specimens with a crack length of 25 and 30 mm, a span length of 50, 55 and 61 mm were selected, respectively.

The selection of the crack angle (β) followed the relationships between the geometry factors (i.e., Y_{I} and Y_{II}) and crack angle for various combinations of a/R and s/R, which are shown in Fig. 3. The corresponding geometry factors of the SCB specimens used in the study are listed in Table 1 [22]. To study the effect of geological anisotropy on fracture behaviour, transversely isotropic bedding planes with three principal orientations with respect to the loading direction (i.e., arrester orientation, Fig. 2a; divider orientation, Fig. 2b; and short transverse orientation, Fig. 2c) were added into the specimens. The spacing of the bedding planes (*d*) remained the constant, which was 17.5 mm [23].

3.2 Calibration

Calibration of the particulate DEM model in this study involved the selection of micro-parameters of SJCM and FJCM. As described earlier, an incipient bedding plane with a direct tensile strength of 1.82 MPa (87.5% intact parent rock strength) was mimicked in the study. The smooth joint properties corresponding to this bedding plane have been calibrated by Shang et al. [23] and are listed in Table 2. While in the calibration of FJCM, the procedure used by Shang et al. [19] was followed, in which uniaxial compressive tests were performed on medium-grained MGS specimens. Fig. 4a shows a representative axial stress-strain curve (black) and this curve was used for the

ACCEPTED MANUSCRIPT

calibration of FJCM. A cylindrical DEM specimen with the same size (88 mm in length and 37 mm in diameter) as that used in the laboratory was generated. The DEM specimen was uniaxially compressed at a constant loading rate of 0.005 m/s through a trial-and-error process until the numerical results matched well with the experimental results. Fig. 4a shows a comparison of the reprenentative stress-strain curves obtained in the laboratory test and DEM simulation. It can be seen that the simulated Young's modulus and peak strength agreed well with those measured from the laboratory experiment. The laboratory sample exhibited a clear shear failure pattern (Fig. 4b), which was however difficult to be reproduced in the DEM simulation (Fig. 4c). The main reason for the discrepancy between the simulated and experimental failure patterns is that the micro-cracks generated within the flat-jointed DEM model cannot coalesce easily and particle rotations were significantly suppressed due to the existence of the flat interfaces after bond failure [20], thus the split shear failure is difficult to be observed in the flat-jointed DEM model. Table 2 shows the corresponding calibrated micro-parameters. Apart from the above micro-parameters (need calibration), in the FJCM, some parameters are determined based on specific situations [19]. In this study, the flat-joint bonded and gapped fraction were set to 1 and 0, respectively, to assume that there were no initial micro-cracks in the DEM specimens. Minimum values of the radial and circumferential elements (1 and 3, respectively) were used to reduce the calculation time [24].

To understand the failure characteristics of MGS under splitting, a numerical Brazilian tension test was additionally performed using the calibrated micro-parameters listed in Table 2. A Brazilian tensile strength of 2.7 MPa was simulated which matched well with experimental result (2.4 MPa [15]). The diametrical splitting failure pattern simulated in the Brazilian test agreed well with that observed in the laboratory (Fig. 5), although a compression-induced failure close to the top platen was also observed in the experiment (Fig. 5a).

4. Numerical results

4.1 Axial load versus deflection

ACCEPTED MANUSCRIPT

Fig. 6 shows representative axial load-deflection plots (*a*/*R*=0.5 and *s*/*R*=0.55), which are typical unimodal curves. The planar anisotropy (i.e., bedding planes) were bedded in three principal orientations, as demonstrated by the insert diagrams (Figs. 6b-6d). Numerical results based on intact isotropic SCB specimens were included for comparison (Fig. 6a). The crack inclination angle, β, was varied from 0° to 46° for this case (*a*/*R*=0.5 and *s*/*R*=0.55) to allow different modes of fracture toughness to be involved (i.e., modes I and II and mixed-mode) [22].

As shown in Fig. 6, all axial loads were increased continuously until clear peak loads were reached; also for most curves, the peak loads increased with the increase of crack inclinations. The measured peak loads were used in the calculation of fracture toughness, which will be presented and discussed in Section 4.2. It was also observed that the curves within the pre-peak regions exhibited a quasi-linear behaviour, which is similar to the experimental observations in the fracture toughness tests on notched deep beam sandstones [25] and SCB Kimachi sandstones [9]. The non-linear behavior (cumulative deformation) observed in the laboratory experiments can be related to the compaction of micro-pores [26], as well as the pre-cut cracks [27] within the specimens used. The present study, however, hypothesize that the quasi-linear behavior observed in the pre-peak region in this DEM study was mainly due to the insignificant closure of the cracks, since there is wide acceptance of the fact that compaction of rock matrix or pores observed in the laboratory is extremely difficult to come by in the particle-based DEM simulations [19, 20, 23].

The post-peak curves in the study however exhibited three different responses. The first response consisted of a clear peak load and an abrupt load drop to the test end. This response appeared for all cases of intact MGS (β=0° - 46°, Fig. 6a) and few cases of horizontally bedded MGS (arrester) with relatively lower crack inclinations (e.g., β=0° and 10°, Fig. 6b). In literature, the abrupt failure response in fracture toughness experiments has been consistently observed [12, 25, 28], which is associated with the brittle nature of rocks. The second response also demonstrated a clear peak, followed however by significant load fluctuations until the complete failure of the

ACCEPTED MANUSCRIPT

specimens (see β=35° - 46° in Fig. 6b and β=0° - 30° in Fig. 6c). The observed load fluctuation was related to the strength difference between the bedding planes and the rock matrix, leading to a complex load-deflection curve. In the third response mode, two load drops in the post-peak regions were observed (e.g., β=45°, Fig. 6d); and the first load drop following the peak load was much smaller than the second one. The load fluctuations observed in this response was due to the fact that the vertically orientated bedding planes with the same direction as that of the applied load significantly affected the integrity of the tested specimens. Particularly, the load-deflection response of the case β=10° (Fig. 6d) exhibited more uncertainties, for which the bedding planes dominated the failure pattern, which will be examined further in Section 4.3.

4.2 Broad-spectrum peak loads and effective fracture toughness

The effective fracture toughness (EFT) of MGS with a broad-spectrum magnitudes ranging between 0.1 and 0.6 MPa $m^{1/2}$ is shown in Fig. 7, where peak loads, in a wide range between 250 and 2000 N, are also included. The crack angles corresponding to mode II fracture toughness for each combination of s/R and a/R are marked blue in the figure.

The simulated peak loads increased gradually with the increase of crack inclinations, but with different extents which was mainly affected by crack length, as shown in Fig. 7. A wider range of peak loads (1.0-2.0 kN, Figs. 7g and 7h) was observed for DEM specimens with a smaller crack length (a/R=0.4), in comparison with that (0.75-1.5 kN, see Figs. 7a-7c) measured by using the specimens with a larger crack length (a/R=0.6). The EFT, however, decreased gradually for all cases when the crack inclination, β, was increased from 0° to a specific angle reflecting mode II fracture toughness. It can also be seen in Fig. 7 that the DEM specimens with short transverse planar anisotropy exhibited relatively smaller EFT (blue dots) compared with those values measured using the specimens with arrester and divider planer anisotropy (red and green dots, respectively). Similar observations have been reported for Mancos shale [3]; however, in their study only mode I fracture toughness was investigated. Additionally, a clear load drop was observed in

ACCEPTED MANUSCRIPT

this study for the short transverse scenarios when the crack inclination β was increased from 0° to 10°. For example, as shown in Fig. 7e, the peak load measured under the mode I level (β=0°) was 0.75 kN, it was then deceased to around 0.43 kN when the crack inclination β was increased to 5°; a further decrease (just below 0.35) was observed when β=10°. After that the peak load was gradually increased with the increase in crack inclination. The peak load reduction described above was probably attributed to the deflection of induced fractures into weaker bedding planes, leading to a smaller peak load [4].

To further understand the effects of crack length (a/R) and span length (s/R) on EFT, the broad range values of EFT (in Fig. 7) were plotted against mode I fracture toughness for different crack lengths (Fig. 8a) and span lengths (Fig. 8b), without showing the effect of geological anisotropy. It can be seen that the EFT reported in this study was approximately linearly correlated with the mode I fracture toughness, irrespective of crack length and span length. More interestingly, somewhat larger values of EFT (0.4-0.6 MPa $m^{1/2}$) were measured for specimens with relatively large crack length (i.e., 30 mm, sky blue dots in Fig. 8a); and fracture toughness of specimens with smaller cracks (20 mm) clustered within the range between 0.1 and 0.35 MPa $m^{1/2}$ (blue dots in Fig. 8a). This cluster phenomenon, however, was not observed in Fig. 8b, where span length was differentiated.

4.3 Failure characteristics

Representative failure characteristics of MGS specimens under mixed-mode loading are shown in Figs. 9-12, where s/R=0.5 and a/R=0.55. Planar anisotropy was oriented in three principal orientations relative to the load direction and the crack inclination angle was varied between 0° and 46°. The failure patterns revealed in the DEM simulations were compared with experimental observations reported in literature. Fig. 9a shows the failure patterns of intact MGS specimens containing a crack with different inclinations. Tensile micro-cracks were marked red and shear micro-cracks were shown as black; and the macro-cracks were formed by the initiation and coalescence of the micro-cracks. Fracture initiation angle θ_0 was illustrated in

ACCEPTED MANUSCRIPT

Fig. 9a (see β=40°). The numerical results in the study showed that the macro-cracks were induced between the tips of the pre-existing cracks and the loading points (see Fig. 9a); and all these macro-cracks were not planar in shape but showed some curvatures, which were quite similar in pattern to the experimental observations (Fig. 9b) [29]. Simulation results also revealed that the micro-mechanical failure of rock matrix/particles involved both tensile and shear micro-cracks (see the failure planes in Fig. 9a). This observation agreed with Backers et al. [30] and Backers and Stephansson [31], who argued that fracturing rock always involved a mixed mode pattern at micro-scale.

The failure patterns of MGS specimens containing arrester planar anisotropy are shown in Figs. 10a-10i. It can be seen that the induced macro-fractures were similar in shape to those generated within the intact MGS specimens (Fig. 9a), although some slight diversion of the fracture planes can be observed (see Figs. 10a, 10c and 10d). The observed diversion are attributed to the geological anisotropy, i.e., the arrester bedding planes affected the integrity of the DEM specimens. The slight diversion in fracture plane orientation was also observed by Lee et al. [11] in their investigation of fracture toughness of veined shale (see Fig. 10k). As it is anticipated that for SCB specimens with arrester planar anisotropy, the induced macro-cracks did not divert into the weakness planes, but were developed and passed through the anisotropic plane (Fig. 10i). This phenomenon was similarly observed in other geo-materials such as bedded coal (Fig. 10j) [32] and a Chinese sandstone (Fig. 10m) [27].

The failure patterns of MGS specimens containing divider planar anisotropy are presented in Fig. 11, in which it can be seen that the macro-fractures were similar in shape in comparison with those observed in Figs. 9 and 10. For the mode I case (Fig. 11, β=0°), the macro-fracture initiated at the tip of the pre-existing crack but propagated with relatively large diversion compared with that observed in Fig. 10a, leading to an irregular-shaped macro-fracture. The pure mode II fracture toughness was measured when β=46° (Fig. 11); and a perfect curved failure plane was generated. As previously described, the mixed-mode fracture toughness was achieved by varying β from 10° to 45°, as shown in Fig. 11. To allow a 3D observation of the internal structure, a top

ACCEPTED MANUSCRIPT

view of a DEM specimen with β =30° (see Fig. 11 at the right corner) is presented, where particles are not shown for clarity. The bedding planes and the induced macro-fracture, as well as a thin section along the pre-existing crack are included. It clearly can be seen that the induced macro-fracture consisted of both tensile and shear micro-cracks (as discussed earlier); also the generated fracture crossed the bedding planes. It is important to note that although the failure patterns observed in Figs 9-11 only exhibited slight differences, such insignificant differences have led to a significant difference in the magnitude peak load, which was sensitive to the external conditions (Fig. 7).

As shown in Fig. 7 and discussed in Section 4.2, much smaller peak loads and EFT were measured for MGS specimens having short transverse planar anisotropy. Some typical failure patterns of MGS specimens with short transverse bedding planes are shown in Fig. 12. As can be seen in this figure, for the case β=0°, the failure characteristic was very similar to that of intact rock (Fig. 9a, β=0°). While a significant diversion failure along an adjacent bedding plane was observed when β was increased up to 10° (see the close-up view in Fig. 12, β=10°). The diversion failure has led to a dramatic drop of peak load, as shown in Fig.7e (blue dots). However, no significant failures along the bedding planes were observed when β were further increased to 30° and 45°; instead, the macro-cracks passed through the planar anisotropy (Fig. 12, β=30°and 45°). It is important to note that this observed failure pattern was depended on the strength/incipiency of bedding planes used in the study. A discussion in this regard will be offered in Section 6, during which bedding planes with a smaller tensile strength was examined. Another interesting observation was that the fracture initiation point for case β=45° (Fig. 12) was not exactly from the tip of the pre-existing crack but from the side which was slightly below the tip. This type of complex fracture propagation was also observed by Lee et al. [11].

To further understand the deformation of the MGS specimens under mixed-mode loading, an example of velocity distribution of particles is shown in Fig. 13, with an emphasis of the areas close to the pre-existing cracks (shown in the close-up views). The particles are shown as arrows with directions. As can

ACCEPTED MANUSCRIPT

be seen in Fig. 13a, the velocity of particles was not equally distributed; the particles around the pre-existing crack on the top section of the specimen exhibited a much smaller velocity (~1.0e^{-3} ms^{-1}) compared with that of particles (~1.0e^{-2} ms^{-1}) on the base of the specimen. As can be anticipated that the particles on the two sides of the pre-existing cracks moved in opposite directions, leading to the gradual opening of the pre-existing cracks, thereby the generation of the macro-fractures. For the specimens with bedding planes distributed in arrester (Fig. 13b) and divider (Fig. 13c) orientations, the velocity directions of the particles were affected by the orientations of the bedding planes and the magnitudes of the particle velocity of these two cases increased in general in comparison with that observed in Fig. 13a. For the case with the short transverse oriented beds (Fig. 13d), a larger range of particle velocity was observed for most of the particles (up to 3.2 e^{-2} ms^{-1}, represented by yellow arrows), which probably can be attributed to the deformation of the short transverse bedding planes.

5. Theoretical analysis of the mixed-mode fracture behaviour of MGS and comparison study

In literature, several fracture criteria have been proposed and used to predict mixed-mode fracture behaviour of solid materials [10, 33-36]. In this section, the mixed-mode fracture toughness of semi-circular MGS specimens was examined by using four different fracture criteria, which are based on stress and strain analysis, and the analysis of energy density. Specifically, the mixed-mode fracture toughness was expressed in the form of K_{Ic}/K_E (for comparison purpose) based on the criteria including generalized maximum tangential stress (GMTSS) criterion, conventional maximum tangential stress (CMTSS) criterion, generalized maximum tangential strain (GMTSN) criterion and generalized average strain energy density (GASED). The predictions of fracture initiation angle and effective fracture toughness required to validate the numerical results were reported.

5.1 Prediction of mixed-mode fracture behaviour based on fracture criteria

ACCEPTED MANUSCRIPT

5.1.1. Fracture behaviour predictions based on the GMTSS and CMTSS criteria

According to the Linear Elastic Fracture Mechaincs (LEFM), the elastic tangential stress, $\sigma_{\theta\theta}$, in the vicinity of a crack tip subjected to mixed-mode loading can be written as [36]

$$\sigma_{\theta\theta} = \frac{1}{\sqrt{2\pi r}} \cos\frac{\theta}{2}\left(K_{\mathrm{I}} \cos^2\frac{\theta}{2} - \frac{3}{2} K_{\mathrm{II}} \sin\theta\right) + T\sin^2\theta + O(r^{1/2}) \tag{4}$$

where r and θ represent the polar coordinates with the origin at the crack tip.

In the GMTSS criterion, it is assumed that crack growth initiates radially from the crack tip along a specific direction of θ_0 (i.e., fracture initiation angle). Crack extension takes place when the tangential stress $\sigma_{\theta\theta}$ along θ_0 and at a critical distance r_c from the crack tip reaches a critical value $\sigma_{\theta\theta c}$. Both r_c and $\sigma_{\theta\theta c}$ are assumed to be material properties (i.e., they are constants for a specific solid material). It is noted that the CMTSS criterion only takes into account the singular term (i.e., $\frac{1}{\sqrt{2\pi \mathrm{r}}} \cos\frac{\theta}{2}\left(K_{\mathrm{I}} \cos^2\frac{\theta}{2} - \frac{3}{2} K_{\mathrm{II}} \sin\theta\right)$) in Eq. (4) [37]. However in the GMTSS criterion, the effect of *T*-stress is also considered in addition to the singular term.

According to the GMTSS criterion, one can obtain

$$\left.\frac{\partial \sigma_{\theta\theta}}{\partial \theta}\right|_{\theta=\theta_0} = 0 \tag{5}$$

Thus, the fracture initiation angle θ_0 under mixed-mode loading is determined from

$$[K_{\mathrm{I}} \sin\theta_0 + K_{\mathrm{II}}(3\cos\theta_0 - 1)] - \frac{16T}{3}\sqrt{2\pi r_c}\cos\theta_0 \sin\frac{\theta_0}{2} = 0 \tag{6}$$

As described earier, the brittle fracture takes place when

$$\sigma_{\theta\theta}(r_c, \theta_0) = \sigma_{\theta\theta c} \tag{7}$$

By replacing the angle θ_0 from Eq. (6) into Eq. (7), the fracture is predicted to initiate when

ACCEPTED MANUSCRIPT

$$\sqrt{2\pi r_c}\sigma_{\theta\theta c} = \cos\frac{\theta_0}{2}(K_{\mathrm{I}}\cos^2\frac{\theta_0}{2} - \frac{3}{2}K_{\mathrm{II}}\sin\theta_0) + \sqrt{2\pi r_c}T\sin^2\theta \tag{8}$$

To further study the fracture initiation angle and onset fracture, two biaxiality ratio, *B* and *α*, are defined as follows [36, 37]:

$$B = T\sqrt{\pi a} / K_{\mathrm{E}} \tag{9}$$

$$\alpha = \sqrt{\frac{2r_c}{a}} \tag{10}$$

It is noted that *B* is geometry factor and its values for SCB specimens with different *a*/*R* and *s*/*R* have been deduced by Ayatallahi and Aliha [22] and are shown in Table 1.

Eq. (8) can be rewritten in terms of $B\alpha$ and K_{Ic}

$$K_{\mathrm{Ic}} = \cos\frac{\theta_0}{2}(K_{\mathrm{I}}\cos^2\frac{\theta_0}{2} - \frac{3}{2}K_{\mathrm{II}}\sin\theta_0) + B\alpha K_{\mathrm{E}}\sin^2\theta_0 \tag{11}$$

Thus, one can get

$$\frac{K_{\mathrm{Ic}}}{K_{\mathrm{E}}} = \frac{1}{K_{\mathrm{E}}}[\cos\frac{\theta_0}{2}(K_{\mathrm{I}}\cos^2\frac{\theta_0}{2} - \frac{3}{2}K_{\mathrm{II}}\sin\theta_0)] + B\alpha\sin^2\theta_0 \tag{12}$$

Replacing Eqs. (1), (2), (9), (10) into Eq. (12), the relationship between K_{Ic} and K_{E} can be rewritten in terms of geometry factors Y_{I}, Y_{II}, and T^* as

$$\frac{K_{\mathrm{Ic}}}{K_{\mathrm{E}}} = \frac{1}{\sqrt{Y_{\mathrm{I}}^2 + Y_{\mathrm{II}}^2}}[\cos\frac{\theta_0}{2}(Y_{\mathrm{I}}\cos^2\frac{\theta_0}{2} - \frac{3}{2}Y_{\mathrm{II}}\sin\theta_0) + T^*\sqrt{\frac{2r_{\mathrm{c}}}{a}}\sin^2\theta_0] \tag{13}$$

Similarly, substituting Eqs. (1) and (3) into Eq. (6), the fracture initiation angle θ_0 under mixed-mode loading can be rewritten in terms of geometry factors Y_{I}, Y_{II}, and T^* as

$$Y_{\mathrm{I}}\sin\theta_0 + Y_{\mathrm{II}}(3\cos\theta_0 - 1) - \frac{16T^*}{3}\sqrt{\frac{2r_{\mathrm{c}}}{a}}\cos\theta_0\sin\frac{\theta_0}{2} = 0 \tag{14}$$

Thereby the Eqs. (13) and (14) can be used to predict the mixed-mode effective fracture toughness K_{E} and the fracture initiation angle θ_0,

ACCEPTED MANUSCRIPT

respectively. The CMTSS criterion can be obtained when T^* in the Eqs. (13) and (14) are ignored (i.e., T^*=0).

5.1.2. Fracture behaviour prediction based on the GMTSN criterion

It is also known that the elastic radial stress, σ_{rr} , in the vicinity of a crack tip subjected to mixed-mode loading can be written as [36]

$$\sigma_{rr}=\frac{1}{\sqrt{2\pi r}}\cos\frac{\theta}{2}[K_{\mathrm{I}}(1+\sin^2\frac{\theta}{2})+K_{\mathrm{II}}(\frac{3}{2}\sin\theta-2\tan\frac{\theta}{2})]+T\cos^2\theta+O(r^{1/2}) \quad (15)$$

According to the Hooke's Law and combining Eqs. (4) and (15), the tangential strain, $\varepsilon_{\theta\theta}$, in the vicinity of the crack can be written as

$$\varepsilon_{\theta\theta}=\frac{1+\upsilon}{E}[k\sigma_{\theta\theta}+(k-1)\sigma_{rr}]=\frac{1+\upsilon}{E\sqrt{2\pi r}}[K_{\mathrm{I}}f_1(\theta)+K_{\mathrm{II}}f_2(\theta)+T\sqrt{2\pi r}f_3(\theta)] \quad (16)$$

where $k=1/(1+\upsilon)$ represents plane stress condition and $k=(1-\upsilon)$ stands for plane strain condition; E and υ are the Young's modulus and Poisson's ratio, respectively. $f_1(\theta)=\frac{1}{4}[(8k-5)\cos\frac{\theta}{2}+\cos\frac{3\theta}{2}]$,

$f_2(\theta)=-\frac{1}{4}[(8k-5)\sin\frac{\theta}{2}+3\sin\frac{3\theta}{2}]$ and $f_3(\theta)=k-\cos^2\theta$.

According to the GMTSN criterion, crack growth initiates radially from the crack tip along the direction of θ_0; and crack extension takes place when the tangential strain $\varepsilon_{\theta\theta}$ along θ_0 and at a critical distance r_c from the crack tip attains a critical value $\varepsilon_{\theta\theta c}$. Both r_c and $\varepsilon_{\theta\theta c}$ are assumed to be material properties. The GMTSN criterion can be expressed as

$$\begin{cases}\left.\dfrac{\partial\varepsilon_{\theta\theta}}{\partial\theta}\right|_{\theta=\theta_0}=0\\ \varepsilon_{\theta\theta}(r_c,\theta_0)=\varepsilon_{\theta\theta c}\\ \left.\dfrac{\partial^2\varepsilon_{\theta\theta}}{\partial\theta^2}\right|_{\theta=\theta_0}<0\end{cases} \quad (17)$$

Replacing Eq. (16) into Eq. (17), the fracture initiation angle θ_0 in terms of geometry factors (Y_{I} and Y_{II}) can be written as

ACCEPTED MANUSCRIPT

$$Y_{\mathrm{I}}[(5-8k)\sin\frac{\theta_0}{2}-3\sin\frac{3\theta_0}{2}]+Y_{\mathrm{II}}[(5-8k)\cos\frac{\theta_0}{2}-9\cos\frac{3\theta_0}{2}] +8B\alpha\sqrt{Y_{\mathrm{I}}^2+Y_{\mathrm{II}}^2}\sin 2\theta_0=0 \tag{18}$$

Substituting the fracture initiation angle θ_0 (obtained form Eq. 18) and Eqs. (2) (9) and (10) into Eq. (16), one can obtain

$$\varepsilon_{\theta_0\theta_0}E\sqrt{2\pi r_c}=(1+\upsilon)[K_{\mathrm{I}}f_1(\theta_0)+K_{\mathrm{II}}f_2(\theta_0)+B\alpha K_{\mathrm{E}}f_3(\theta_0)] \tag{19}$$

For the conventional mode I loading condition, $K_{\mathrm{I}}=K_{\mathrm{Ic}},K_{\mathrm{II}}=0$ and $\theta_0=0$, the following equaiton can be obtained according to Eqs. (17) and (19).

$$\varepsilon_{\theta_0\theta_0}E\sqrt{2\pi r_c}=(1+\upsilon)[(2k-1)+B\alpha(k-1)]K_{\mathrm{Ic}}\,,\ (B\alpha-\frac{(2k-1)}{8}<0) \tag{20}$$

Combining Eqs. (19) and (20), one can obtain

$$\begin{aligned}&K_{\mathrm{I}}f_1(\theta_0)+K_{\mathrm{II}}f_2(\theta_0)+B\alpha K_{\mathrm{E}}f_3(\theta_0)\\&=[(2k-1)+B\alpha(k-1)]K_{\mathrm{Ic}}\end{aligned}\,,\ (B\alpha-\frac{(2k-1)}{8}<0) \tag{21}$$

Dividing both sides of Eq. (21) by K_{E}, the mixed-mode fracture (in the form of $\frac{K_{\mathrm{Ic}}}{K_{\mathrm{E}}}$) can be predicted and written in terms of geometry factors (Y_{I} and Y_{II}) as

$$\frac{K_{\mathrm{Ic}}}{K_{\mathrm{E}}}=\frac{(\frac{Y_{\mathrm{I}}f_1+Y_{\mathrm{II}}f_2}{\sqrt{Y_{\mathrm{I}}^2+Y_{\mathrm{II}}^2}})+B\alpha f_3}{(2k-1)+B\alpha(k-1)}\,,\ (B\alpha-\frac{(2k-1)}{8}<0) \tag{22}$$

5.1.3. Fracture behaviour prediction based on the GASED criterion

For the plane elasticity problems, the strain energy density function, $\mathrm{dW/dV}$, stored in an element can be written as [38]

$$\mathrm{dW/dV}=\frac{1}{2G}[\frac{m+1}{8}(\sigma_{rr}+\sigma_{\theta\theta})^2-\sigma_{rr}\sigma_{\theta\theta}+\sigma^2_{r\theta}] \tag{23}$$

where G is the modulus of rigidity and it is known that $G=E/2(1+\upsilon)$. m is an elastic constant and $m=3-4\upsilon, m=\frac{3-\upsilon}{1+\upsilon}$ for plane strain and plane stress problems, respectively.

ACCEPTED MANUSCRIPT

According to Smith et al. [36] and the Airy stress function proposed by Williams [39], the stress $\sigma_{r\theta}$ in the vicinity of a crack tip subjected to mixed-mode loading can be written as

$$\sigma_{r\theta}=\frac{1}{2\sqrt{2\pi r}}\cos\frac{\theta}{2}[K_{\mathrm{I}}\sin\frac{\theta}{2}+K_{\mathrm{II}}(3\cos\theta-1)]-T\sin\theta\cos\theta+O(r^{1/2}) \qquad (24)$$

The average strain energy density factor *S*, reflecing the strength of the elastic energy field in the vicinity of the crack tip, is defined as [38]

$$S=r\mathrm{dW}/\mathrm{dV} \qquad (25)$$

Substituting the stress components from Eqs. (4), (15), (23) and (24) into Eq. (25), the following can be derived

$$\begin{aligned} S &= A_1 K_{\mathrm{I}}{}^2 + A_2 K_{\mathrm{II}}{}^2 + 2A_3 K_{\mathrm{I}} K_{\mathrm{II}} + 2A_4 T K_{\mathrm{I}}\sqrt{2\pi r} \\ &\quad + 2A_5 T K_{\mathrm{II}}\sqrt{2\pi r} + A_6 2\pi r T^2 \end{aligned} \qquad (26)$$

where

$$\begin{cases} A_1 = \dfrac{1}{16\pi G}[(m-\cos\theta)(1+\cos\theta)] \\ A_2 = \dfrac{1}{16\pi G}[m(1-\cos\theta)+\cos\theta(1+3\cos\theta)] \\ A_3 = \dfrac{1}{16\pi G}\sin\theta(2\cos\theta-m+1) \\ A_4 = \dfrac{1}{16\pi G}\cos\dfrac{\theta}{2}(\cos 2\theta-\cos\theta+m-1) \\ A_5 = -\dfrac{1}{16\pi G}\sin\dfrac{\theta}{2}(\cos 2\theta+\cos\theta+m+1) \\ A_6 = \dfrac{1}{16\pi G}(\dfrac{m+1}{2}) \end{cases} \qquad (27)$$

According to the GASED criterion, crack growth initiates radially from the crack tip along the direction of θ_0 where the amount of the strain energy density factor is minimum at a critical distance r_c from the crack tip. The GASED criterion can be expressed as

$$\left.\frac{\partial S}{\partial\theta}\right|_{\theta=\theta_0}=0 \qquad (28)$$

ACCEPTED MANUSCRIPT

Thus the fracture initiation angle θ_0 can be determined and written in terms of the geometry factors (Y_{I} and Y_{II}) using the following equations

$$\begin{aligned} &C_1 Y_{\mathrm{I}}^2 + C_2 Y_{\mathrm{II}}^2 + C_3 Y_{\mathrm{I}} Y_{\mathrm{II}} + C_4 B\alpha Y_{\mathrm{I}} \sqrt{Y_{\mathrm{I}}^2 + Y_{\mathrm{II}}^2} \\ &+ C_5 B\alpha Y_{\mathrm{II}} \sqrt{Y_{\mathrm{I}}^2 + Y_{\mathrm{II}}^2} + C_6 (B\alpha)^2 (Y_{\mathrm{I}}^2 + Y_{\mathrm{II}}^2)^2 = 0 \end{aligned} \tag{29}$$

where

$$\begin{cases} C_1 = \dfrac{1}{16\pi G} \sin\theta_0 (2\cos\theta_0 - m + 1) \\ C_2 = -\dfrac{1}{16\pi G} \sin\theta_0 (6\cos\theta_0 - m + 1) \\ C_3 = \dfrac{1}{8\pi G} (2\cos 2\theta_0 - m\cos\theta_0 + \cos\theta_0) \\ C_4 = -\dfrac{1}{16\pi G} \sin\dfrac{\theta_0}{2} (5\cos 2\theta_0 + \cos\theta_0) + m + 1) \\ C_5 = -\dfrac{1}{16\pi G} \cos\dfrac{\theta_0}{2} (5\cos 2\theta_0 - \cos\theta_0) + m + 3) \\ C_6 = 0 \end{cases} \tag{30}$$

According to the GASED criterion, fracture takes place when S reaches its critical value S_{c}

$$S = S_{\mathrm{c}} \tag{31}$$

Substituting the fracture initiation angle θ_0 (obtained form Eq. 29) and Eqs. (2), (9), (10) and (26) into Eq. (31), the fracture can be predicted by

$$\begin{aligned} S_c = {} & A_1 K_{\mathrm{I}}^2 + A_2 K_{\mathrm{II}}^2 + A_3 K_{\mathrm{I}} K_{\mathrm{II}} + A_4 B\alpha K_{\mathrm{E}} K_{\mathrm{I}} \\ & + A_5 B\alpha K_{\mathrm{E}} K_{\mathrm{II}} + A_6 (B\alpha K_{\mathrm{E}})^2 \end{aligned} \tag{32}$$

S_{c} is a constant material property and as described by Sih [35], this property can be expressed by

$$S_c = \frac{1}{8\pi G} (m-1) K_{\mathrm{Ic}}^2 \tag{33}$$

Thus

$$\begin{aligned} \frac{1}{8\pi G} (m-1) K_{\mathrm{Ic}}^2 = {} & A_1 K_{\mathrm{I}}^2 + A_2 K_{\mathrm{II}}^2 + A_3 K_{\mathrm{I}} K_{\mathrm{II}} + A_4 B\alpha K_{\mathrm{E}} K_{\mathrm{I}} \\ & + A_5 B\alpha K_{\mathrm{E}} K_{\mathrm{II}} + A_6 (B\alpha K_{\mathrm{E}})^2 \end{aligned} \tag{34}$$

ACCEPTED MANUSCRIPT

Dividing both sides of Eq. (34) by K_E^2, the mixed-mode fracture (in the form of $\frac{K_{Ic}}{K_E}$) can be predicted and written in terms of geometry factors (Y_I and Y_{II}) as

$$
\begin{aligned}
& A_1\left(\frac{K_{Ic}}{K_E}\right)^2 + A_4 B\alpha \frac{K_{Ic}}{K_E} - A_1\left(\frac{Y_I}{\sqrt{Y_I^2 + Y_{II}^2}}\right)^2 \\
& - A_2\left(\frac{Y_{II}}{\sqrt{Y_I^2 + Y_{II}^2}}\right)^2 - A_3 \frac{Y_I Y_{II}}{Y_I^2 + Y_{II}^2} \\
& - A_4 \frac{B\alpha Y_I}{\sqrt{Y_I^2 + Y_{II}^2}} - A_5 \frac{B\alpha Y_{II}}{\sqrt{Y_I^2 + Y_{II}^2}} = 0
\end{aligned}
\tag{35}
$$

5.2 Comparing the theoretical predictions of mixed-mode fracture behaviour with that from DEM simulations

Figs.14-16 show the infered fracture initiation angle and EFT (in the form of K_E/K_{Ic}) for different combinations of a/R (0.4, 0.5 and 0.6) and s/R (0.5, 0.55 and 0.61). For comparison, the previously reported DEM results are included in those figures and shown as scattered dots. As shown in Fig.14 (a/R=0.4; s/R=0.5 and 0.55, respectively), the DEM simulation results in terms of fracture initiation angle (Figs. 14a and 14c) and EFT (Figs. 14b and 14d) agreed in broad with the predictions by the GMTSS, GMTSN and GASED criteria. Nevertheless, slightly larger discrepancies between the theoretical and numerical predictions still can be observed when the crack angle was between 20° and 35° for the case a/R=0.4 and s/R=0.5 (Fig. 14b), as well as when the crack angle was larger than 50° for the case a/R=0.4 and s/R=0.55 (Fig. 14d). Almost without exception, the CMTSS criterion overestimated EFT and underestimated the fracture initiation angle.

A relatively large degree of discrepency between the theoretical predictions and the numerical results can be observed when a/R was increased to 0.5 (Fig.15), especially when s/R=0.55. For example, as can be seen in Figs. 15b, 15d and 15f, the DEM predicted K_E/K_{Ic} (scattered dots) for the specimens with different orientations of planar anisotropy almost lay between the predictions by the GMTSS criterion and the CMTSS criterion.This observation indicated that the influence of geological anisotropy on fracture behaviour of the SCB specimens used in the study became larger when the crack length a was

ACCEPTED MANUSCRIPT

increased to the half of the specimen diameter R. It also can be seen that, for specimens with short transverse planar anisotropy, three unexpected values of K_E/K_{Ic} were numerically obtained (between 0.5 and 0.7) when crack angles were 5°, 10° and 15°, respectively (Fig. 15d), which were much lower than the theoretical predictions (0.83-0.98).

As shown in Fig. 16, a better match between the simulated fracture behaviour and theoretical predicitons can be seen when a/R was increased further to 0.6, where s/R was varied from 0.5 to 0.61. Again, the CMTSS criterion exhibited poor performance in the prediction of fracture behaviour compared with the other three criteria (i.e., GMTSS, GMTSN and GASED criteria).

6. Discussion

The fracture toughness of rock materials can be measured in the laboratory using the specimens recommended by ISRM (i.e, SCB, SR and CBD specimens). The reliability of the laboratory-scale measurements however can be affected by many factors including geological anisotropy [3], geometrical properities of the specimens used [6], as well as experimental setup [17]. This fact is widely acknowledged, however it still lacks a systematic study on how these factors affect the fracture behaviour of anisotropic rocks. As such, in this study a comprehensive numerical analysis of the fracture behaviour of MGS was conducted and a broad-spectrum mixed-mode fracture toughness of this lithology was reported based on a total of 340 DEM simulations. The influences of planar anisotropy orientation, length and angle of the pre-existing cracks, as well as span length were considered in the DEM simulation. The DEM results were compared quantitatively with theoretical predictions and qualitatively with previous experimental observations.

Although a broad agreement has been observed in the comparison study (Figs. 14-17), some discrepancies still existed, especially for the cases when a/R=0.5 (Figs. 15b, 15d and 15f). The observed discrepancies can probably be related to: (1) the ignorance of the influence of geological anisotropy on the fracture behaviour of solid materials by the current fracture criteria [34, 36, 38]; and (2) the inherent limitations of the DEM code used in the study (for example, the spherical assembles were used in the present simualtion to

ACCEPTED MANUSCRIPT

represent real rock matrix, which is an assumption) [20, 21]. The frustrating performance of the CMTSS criterion in the prediciton of fracture behaviour was also noted in this study, which is mainly due to the ignorance of the non-singular term in that criterion (i.e., the *T*-stress shown in Eqs. 13 and 14) [37].

Additionally, a diversion failure of fracture from rock matrix to pre-existing bedding planes was observed for short transverse bedded specimens with a relatively small crack inclination angle (i.e., β<15°), which has led to a distinct peak load drop (Fig. 7, blue dots). However, the diversion failure was not observed for arrester and divider bedded specimens, as well as for short transverse bedded specimens with a relatively high crack inclination angle (i.e., β>15°). It is important to note that the bedding planes with a tensile strength of 87.5 % that of parent rock was modelled in the study, thus the above failure observation only applies to the anisotropic rocks with relatively high tensile strength bedding planes/planar anisotropy.

Additional DEM fracture toughness simulations based on the SCB sepcimens (a/R=0.5 and s/R=0.55) containing short transvese bedding planes with a relatively low tensile strength (i.e., bedding planes with a tensile strength of 31.3 % that of parent rock were used [23, 40]). The corresponding micro-parameters of the low-strength bedding plane within MGS has been reported by Shang et al. [23] and are listed in Table 2. The numerical scheme is the same as that described in Section 3.1. The relationship bewteen the axial load and deflection of the four additional simulations is shown in Fig. 17, with the simulated failure patterns (Figs. 17b-17e) and corresponding experimental observations included (Figs. 17f-17h) (The experiment was reported by Roy et al. [14]). It can be seen that the peak load increased with the increasing of the crack inclination angles (β from 0° to 46°, Fig. 17a). As expected, one planar failure plane was generated within the rock matrix when β=0° (Fig.17b), which was very close to the observed patterns shown in Fig.12 (β=0°). At β=20° (Fig.17c), a non-planar failure plane was induced, with a combination failure of the adjacent bedding plane (the failure of bedding planes was represented by the pure tensile micro-cracks shown in red) and the rock matrix close to the loading point. This failure pattern was close to that shown in Fig. 17h, in which the cement joint planes with a similar tensile strength to

ACCEPTED MANUSCRIPT

that of our weak bedding planes were used in the laboratory [14]. Notably, “Z”-shaped failure planes were obseved when β were increased up to 30° (Fig. 17d) and 46° (Fig.17e), respectively. In these two cases, fractures initiated at the pre-existing crack tips, and then propagated within the rock material before reaching the adjacent bedding planes. The pure tensile failures of the bedding planes were then observed (red micro-cracks in Figs.17d and 17e), followed by the failures of the rock materials close to the loading points. Similar observations were achieved by Roy et al. [14] in the laboratory (see Figs. 17f and 17g). It shoud be noted that the origin of the “Z”-shaped failure pattern observed in the study was largely dependent on the relative tensile strength of the planar anisotropy to that of the parent rock.

7. Conclusions

In this paper, a broad-spectrum mixed-mode fracture behaviour of an anisotropic sandstone was reported based on a 3D DEM study, where the ISRM-suggested SCB specimens with different geological and geometrical conditions (i.e., a combination of a/R, s/R, β and orientation of planar anisotropy) were used. The numerical findings of the study were validated against experimental observations and theoretical predictions and a good agreement was observed. Results of the study allow a new insight into the possible variations of the fracture toughness of anisotropic rocks (arising from the factors mentioned above). The main conclusions of this study are shown as follows:

(1) The axial load-deflection curves obtained in this numeircal study exhibited three different responses in the post-peak region: 1) one abrupt load drop (for all specimens without planar anisotropy and few specimens with arrester oriented planar anisotropy); 2) significant load fluctuations until the complete failure of specimens (for most specimens with arrester and divider oriented planar anisotropy); and 3) two load drops (for most specimens with short transverse oriented planar anisotropy).

(2) A broad-spectrum effective fracture toughness (EFT) of Midgley Grit sandstone was revealed, which were between 0.1 and 0.6 MPa $m^{1/2}$. The DEM specimens with short transverse planar anisotropy exhibited relatively

ACCEPTED MANUSCRIPT

small EFT in comparison with those measured using the specimens with arrester and divider planer anisotropy. Furthermore, a distinct drop of EFT was observed in this study for the short transverse bedded specimens when the crack inclination β was increased from 0° to 10°.

(3) It was also concluded that the EFT of Midgley Grit sandstone was approximately linearly correlated with the mode I fracture toughness, irrespective of geological and geometrical conditions. Also, somewhat larger values of EFT (0.4-0.6 MPa $m^{1/2}$) were measured for the specimens with relatively large crack length (i.e., 30 mm in the study), in comparison with those values (0.1-0.35 MPa $m^{1/2}$) measured using the specimens with smaller crack length (20 mm in the study). The effect of span length on the magnitude of EFT was not significant.

(4) For the SCB specimens with a higher tensile strength planar anisotropy (1.82 MPa), the failure characteristics of the specimens in this study exhibited a similar pattern. The non-planar macro-fractures induced in the DEM specimens passed through the anisotropic planes, except for a few specimens containing short transverse planar anisotropy with a relatively low crack inclination angle (β<10°), for which the diversion failure from the rock matrix to the weak planar anisotropy was observed. For specimens with a lower tensile strength anisotropic plane (0.65 MPa in the study), a much more complex failure pattern was observed for specimens containing short transverse planar anisotropy. A complex combination failure of rock matrix and planar anisotropy was observed, leading to a “Z”-shaped failure plane.

References

[1] R. Barati, J. Liang, A review of fracturing fluid systems used for hydraulic fracturing of oil and gas wells, J. Appl. Polym. Sci. 131 (2014) https://doi.org/10.1002/app.40735.

[2] M.E. Hanson, R.J. Shaffer, G.D. Anderson, Effects of various parameters on hydraulic fracturing geometry, SPE 1980 Unconventional Gas Recovery Symposium. Pittsburgh (1980) https://doi.org/10.2118/8942-PA.

ACCEPTED MANUSCRIPT

[3] M.R. Chandler, P.G. Meredith, N. Brantut, B. R. Crawford, Fracture toughness anisotropy in shale, J. Geophys. Res. Solid Earth 121 (2016) 1706–1729.

[4] S.H. Na, W.C. Sun, M.D. Ingraham, H. Yoon, Effects of spatial heterogeneity and material anisotropy on the fracture pattern and macroscopic effective toughness of Mancos Shale in Brazilian tests, J. Geophys. Res. Solid Earth 122 (2017) 6202–6230.

[5] J. Justo, J. Castro, S. Cicero, M.A. Sánchez-Carro, R. Husillos, Notch effect on the fracture of several rocks: Application of the theory of critical distances, Theor. Appl. Fract. Mech. 90 (2017) 251-258.

[6] M.R. Ayatollahi, J. Akbardoost, Size and geometry effects on rock fracture toughness: Mode I fracture, Rock Mech. Rock Eng. 47 (2014) 677-687.

[7] K. Khan, N.A. Al-Shayea, Effect of specimen geometry and testing method on mixed mode I-II fracture toughness of a limestone rock from Saudi Arabia, Rock Mech. Rock Eng. 33 (3) (2000) 179-206.

[8] J.P. Zuo, H.P. Xie, F. Dai, Y. Ju, Three-point bending test investigation of the fracture behaviour of siltstone after thermal treatment, Int. J. Rock Mech. Min. Sci. 70 (2014) 133-143.

[9] T. Funatsu, M. Seto, H. Shimada, K. Matsui, M. Kuruppu, Combined effects of increasing temperature and confining pressure on the fracture toughness of clay bearing rocks, Int. J. Rock Mech. Min. Sci. 41 (2004) 927-938.

[10] M.R.M. Aliha, F. Berto, A. Mousavi, S.M.J. Razavi, On the applicatility of ASED criterion for predicting mixed mode I+II fracture toughness results of a rock material, Theor. Appl. Fract. Mech. 92 (2017) 198-204.

[11] H.P. Lee, J.E. Olson, J. Holder, J.F.W. Gale, R.D. Myers, The interaction of propagating opening mode fractures with preexisting discontinuities in shale, J. Geophys. Res. Solid Earth 120 (2015) 169–181.

[12] K.P. Chong, M.D. Kuruppu, Fracture toughness determination of layered materials, Eng. Fract. Mech. 28 (1) (1987) 43-54.

[13] G.R. Krishnan, X.L. Zhao, M. Zaman, J.C. Roegiersa, Fracture toughness of a soft sandstone, Int. J. Rock Mech. Min. Sci. 35 (6) (1998) 695-710.

[14] D.G. Roy, T.N. Singh, J. Kodikara, Influence of joint anisotropy on the fracturing behaviour of a sedimentary rock, Eng. Geol. 228 (2017) 224-237.

ACCEPTED MANUSCRIPT

[15] J. Shang, S.R. Hencher, L.J. West, Tensile strength of geological discontinuities including incipient bedding, rock joints and mineral veins, Rock Mech. Rock Eng. 49 (11) (2016) 4213-4225.

[16] ISRM, The complete ISRM suggested methods for rock characterization, testing and monitoring: 1974–2006. In: Suggested methods prepared by the commission on testing methods, International Society for Rock Mechanics, compilation arranged by the ISRM Turkish National Group. Kozan Ofset, Ankara (2007).

[17] ISRM, ISRM-suggested method for determining the mode I static fracture toughness using semi-circular bend specimen. In: The ISRM suggested methods for rock characterization, testing and monitoring: 2007–2014, doi: 10.1007/978-3-319-07713-0 (2015).

[18] Y.X. Zhao, S. Gong, X.J. Hao, Y. Peng, Y.D., Jiang, Effects of loading rate and bedding on the dynamic fracture toughness of coal: laboratory experiments, Eng. Frac. Mech. 178 (2017) 375-391.

[19] J. Shang, Y. Yokota, Z. Zhao, W. Dang, DEM simulation of mortar-bolt interface behaviour subjected to shearing, Constr. Build. Mater. Under revision.

[20] D.O. Potyondy, PFC 3D flat joint contact model version 1, Itasca Consulting Group (2013).

[21] J. Shang, Z. Zhao, S. Ma, On the shear failure of incipient rock discontinuities under CNL and CNS boundary conditions: Insights from DEM modelling, Eng. Geol. 234 (21) (2018) 153-166.

[22] M.R. Ayatollahi, M.R.M. Aliha, Wide range data for crack tip parameters in two disc-type specimens under mixed mode loading, Comput. Mater. Sci. 38 (2007) 660-670.

[23] J. Shang, D. Kang, Y. Gui, K. Handley, Z. Zhao, Numerical investigation of the direct tensile behaviour of laminated and transversely isotropic rocks containing incipient bedding planes with different strengths, Comput. Geotech. (2017) doi: https://doi.org/10.1016/j.compgeo.2017.11.007.

[24] Y. Wang, R. Yang, Study of the dynamic fracture characteristics of coal with a bedding structure based on the NSCB impact test, Eng. Frac. Mech. 184 (2017) 319-338.

ACCEPTED MANUSCRIPT

[25] Y. Luo, L. Ren, L.Z. Xie, T. Ai, B. He, Fracture behaviour investigation of a typical sandstone under mixed-mode I/II loading using the notched deep beam bending method, Rock Mech. Rock Eng. 50 (2017) 1987-2005.
[26] J. Shang, J. Hu, K. Zhou, X. Luo, M.M. Aliyu, Porosity increment and strength degradation of low-porosity sedimentary rocks under different loading conditions, Int. J. Rock Mech. Min. Sci. 75 (2015) 216-223.
[27] G. Feng, Y. Kang, F. Chen, Y. Liu, X. Wang, The influences of temperatures on mixed-mode (I+II) and mode-II fracture toughness of sandstone, Eng. Fract. Mech. 189 (2018) 51-63.
[28] M.R.N. Aliha, Gh. R. Hosseinpour, M.R. Ayatollahi, Application of cracked triangular specimen subjected to three-point bending for investigation fracture behaviour of rock materials, Rock Mech. Rock Eng. 46 (2013) 1023-1034.
[29] L. Ren, L.Z. Xie, H.P. Xie, T. Ai, B. He, Mixed-mode fracture behaviour and related surface topography feature of a typical sandstone, Rock Mech. Rock Eng. 49 (2016) 3137-3153.
[30] T. Backers, S. Stanchits, G. Dresen, Tensile fracture propagation and acoustic emission activity in sandstone: the effect of loading rate, Int. J. Rock Mech. Min. Sci. 42 (7-8) (2005) 1094-1101.
[31] T. Backers, O. Stephansson, ISRM suggested method for the determination of Mode II fracture toughness, Rock Mech. Rock Eng. 45 (6) (2012) 1011-1022.
[32] G. Wang, Y. Zhang, Y. Jiang, S. Wang, W. Jing, Macro-micro failure mechanisms and damage modelling of a bolted rock joint, Adv. Mater. Sci. Eng. https://doi.org/10.1155/2017/1627103.
[33] M.R. Ayatollahi, M.R.M. Aliha, Mixed mode fracture in soda lime glass analysed by using the generalized MTS criterion, Int. J. Solids Struct. 46 (2009) 311-321.
[34] W. Hua, S. Dong, X. Pan, Q. Wang, Mixed mode fracture analysis of CCBD specimens based on the extended maximum tangential strain criterion, Fatigue Fract. Eng. Mater. Struct. 40 (2017) 2118-2127.
[35] G.C. Sih, Strain-energy-density factor applied to mixed mode crack problems. Int. J. Fract. 10 (1974) 305-32.

ACCEPTED MANUSCRIPT

[36] D.J. Smith, M.R. Ayatollahi, M.J. Pavier, The role of *T*-stress in brittle fracture for linear elastic materials under mixed mode loading. Fatigue Fract. Eng. Mater. Struct. 24 (2001)137-150.

[37] M. Wei, F. Dai, N. Xu, Y. Liu, T. Zhao, Fracture prediction of rocks under mode I and mode II loading using the generalized maximum tangential strain criterion, Eng. Fract. Mech. 186 (2017) 21-38.

[38] M.R. Ayatollahi, M.R. Moghaddam, F. Berto, A generalised strain energy density criterion for mixed mode fracture analysis in brittle and quasi-brittle materials, Theor. Appl. Fract. Mech. 79 (2015) 70-76.

[39] M.L. Williams, On the stress distribution at the base of a stationary crack, J. Appl. Mech. 24 (1957) 109-114.

[40] J. Shang, S.R. Hencher, L.J. West, Tensile strength of incipient rock discontinuities. Eurock 2015 & 64th Geomechanics Colloquium, Salzburg, Austria (2015) pp. 565-570.

Fig Captions:

Fig. 1 Location (a) and (b) and simplified geological map (c) of the Blackhill Quarry (UK), where the anisotropic Midgley Grit sandstone (d) is mined. (e) A photomicrograph of thin section showing the mineralogy of the Midgley Grit sandstone.

Fig. 2 Numerical setup of semi-circular bend MGS specimens with three principal orientations of planar anisotropy: (a) arrester; (b) divider and (c) short transverse. Close-up of flat joint and flat joint contacts is shown in (a). See text for more details about the geometrical parameters.

Fig. 3 Geometry factors (Y_{I}, Y_{II}, T^* and B) for SCB specimens with various combinations of s/R and a/R. The crack inclinations corresponding to the mode II fracture toughness for each combination are marked in red. (Adapted from [22])

Fig. 4 (a) Comparison of unconfined stress-strain curves of MGS from laboratory test and DEM simulation; (b) failure pattern of an intact MGS after a uniaxial compression test; and (c) failure pattern of a DEM specimen uniaxially compressed.

ACCEPTED MANUSCRIPT

Fig. 5 Comparison of the failure patterns of Brazilian tests: (a) laboratory test and (b) DEM simulation.

Fig. 6 Representative axial load-deflection curves of SCB specimens under mixed-mode loading (a/R=0.5 and s/R=0.55). (a) Intact MGS specimens without planar anisotropy and MGS specimens containing planar anisotropy with three principal orientations: (b) arrester, (c) divider and (d) short transverse.

Fig. 7 Broad-spectrum peak loads and effective fracture toughness of anisotropic semi-circular MGS specimens with various combinations of a/R, s/R and β.

Fig. 8 Effective fracture toughness against mode I fracture toughness for different crack lengths (a) and span lengths (b).

Fig. 9 Failure patterns of SCB sandstone specimens without planar anisotropy: (a) DEM simulations of MGS and (b) laboratory tests on a Chinese sandstone [29]. The fracture initiation angle θ_0 is illustrated on the failed DEM specimen at β=40°.

Fig. 10 (a) Failure characteristics of semi-circular MGS specimens containing arrester planar anisotropy and crack inclination was varied from 0° (a) to 46° (h) in the DEM simulations. A 3D view showing the arrester bedded planar anisotropy and the induced fracture was presented without showing the particles (i). Failure patterns of three different geo-materials with arrester planar anisotropy were included for comparison: (j) bedded coal [24]; (k) veined shale [11] and (m) a bedded Chinese sandstone [27].

Fig. 11 Failure characteristics of semi-circular MGS specimens containing divider planar anisotropy. A 3D top view of the failed specimen with β =30° is presented without showing the particles.

Fig. 12 Typical failure patterns of MGS specimens with short transverse planar anisotropy.

Fig. 13 An illustration of particle velocity (at micro-scale) of semi-circular MGS specimens under mixed-mode loading: (a) a cracked specimen without planar

ACCEPTED MANUSCRIPT

anisotropy (β=30°); cracked specimens with arrester (b), divider (c) and short transverse (d) planar anisotropy. The particles are shown as arrows with orientations.

Fig. 14 Comparison of the numerical results and theoretical predictions: Fracture initiation angle versus crack angle for (a) a/R=0.4, s/R=0.5 and (c) a/R=0.4, s/R=0.55; and effective fracture toughness (in the form of K_E/K_{Ic}) against crack angle for (b) a/R=0.4, s/R=0.5 and (d) a/R=0.4, s/R=0.55.

Fig. 15 Comparison of numerical results and theoretical predictions: Fracture initiation angle versus crack angle for (a) a/R=0.5, s/R=0.5; (c) a/R=0.5, s/R=0.55; and (e) a/R=0.5, s/R=0.61; as well as effective fracture toughness (in the form of K_E/K_{Ic}) against crack angle for (b) a/R=0.5, s/R=0.5; (d) a/R=0.5, s/R=0.55; and (f) a/R=0.5, s/R=0.61.

Fig. 16 Comparison of numerical results and theoretical predictions: Fracture initiation angle versus crack angle for (a) a/R=0.6, s/R=0.5; (c) a/R=0.6, s/R=0.55; and (e) a/R=0.6, s/R=0.61; as well as effective fracture toughness (in the form of K_E/K_{Ic}) against crack angle for (b) a/R=0.6, s/R=0.5; (d) a/R=0.6, s/R=0.55; and (f) a/R=0.6, s/R=0.61.

Fig. 17 (a) Axial load versus deflection of four MGS specimens with weaker short transverse planar anisotropy (i.e., the bedding planes with a direct tensile strength of 31.3 % that of the parent rock). (b) - (d) Failure patterns of the four additional simulations and (f)-(h) similar failure patterns observed by Roy et al. [14] in their laboratory experiments.

ACCEPTED MANUSCRIPT

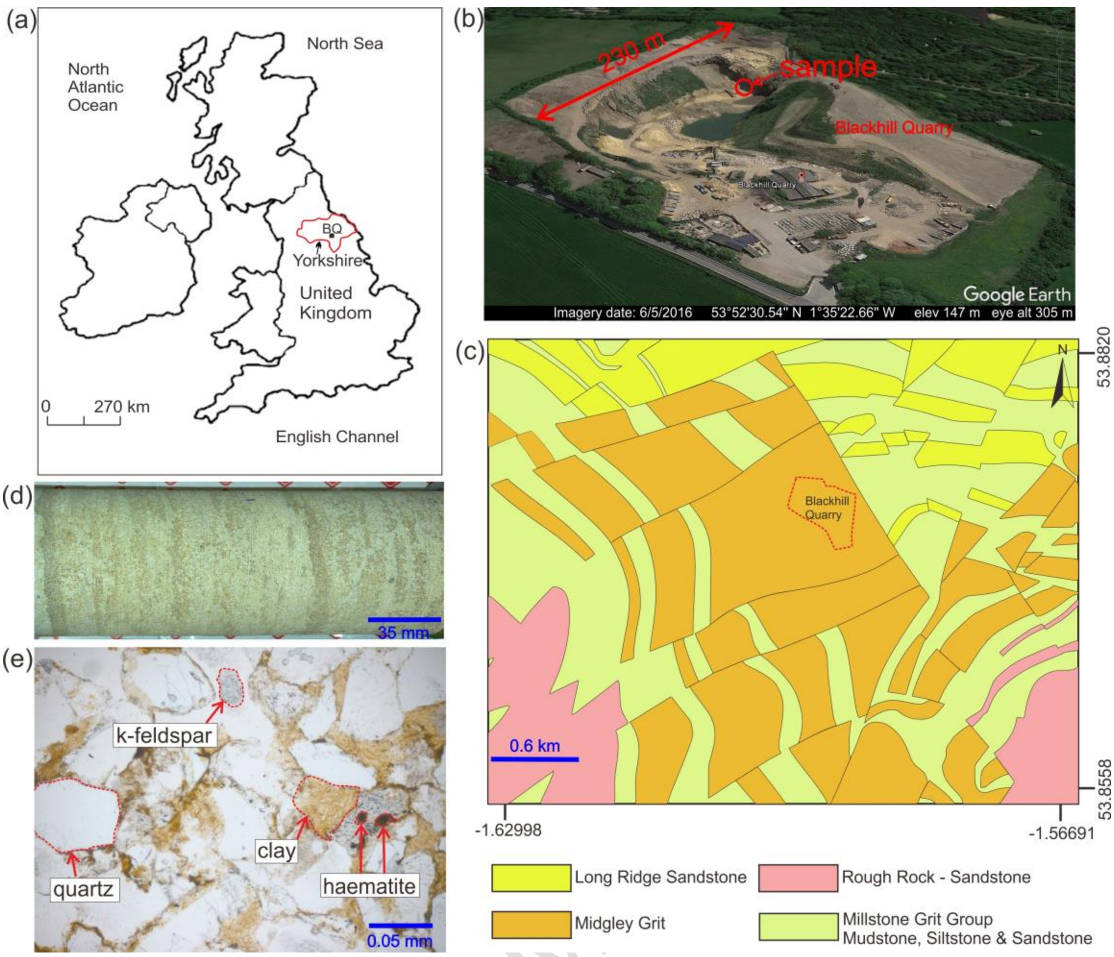

Fig 1

ACCEPTED M

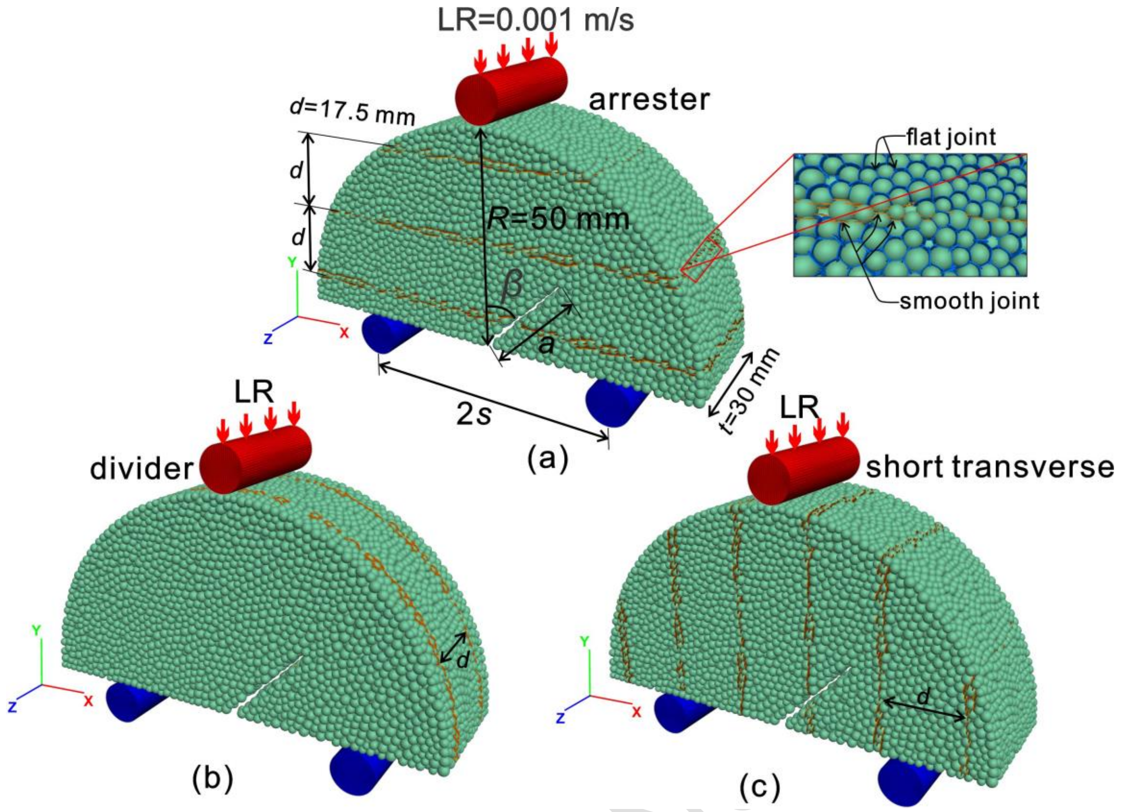

Fig 2

ACCEPTED MANUSCRIPT

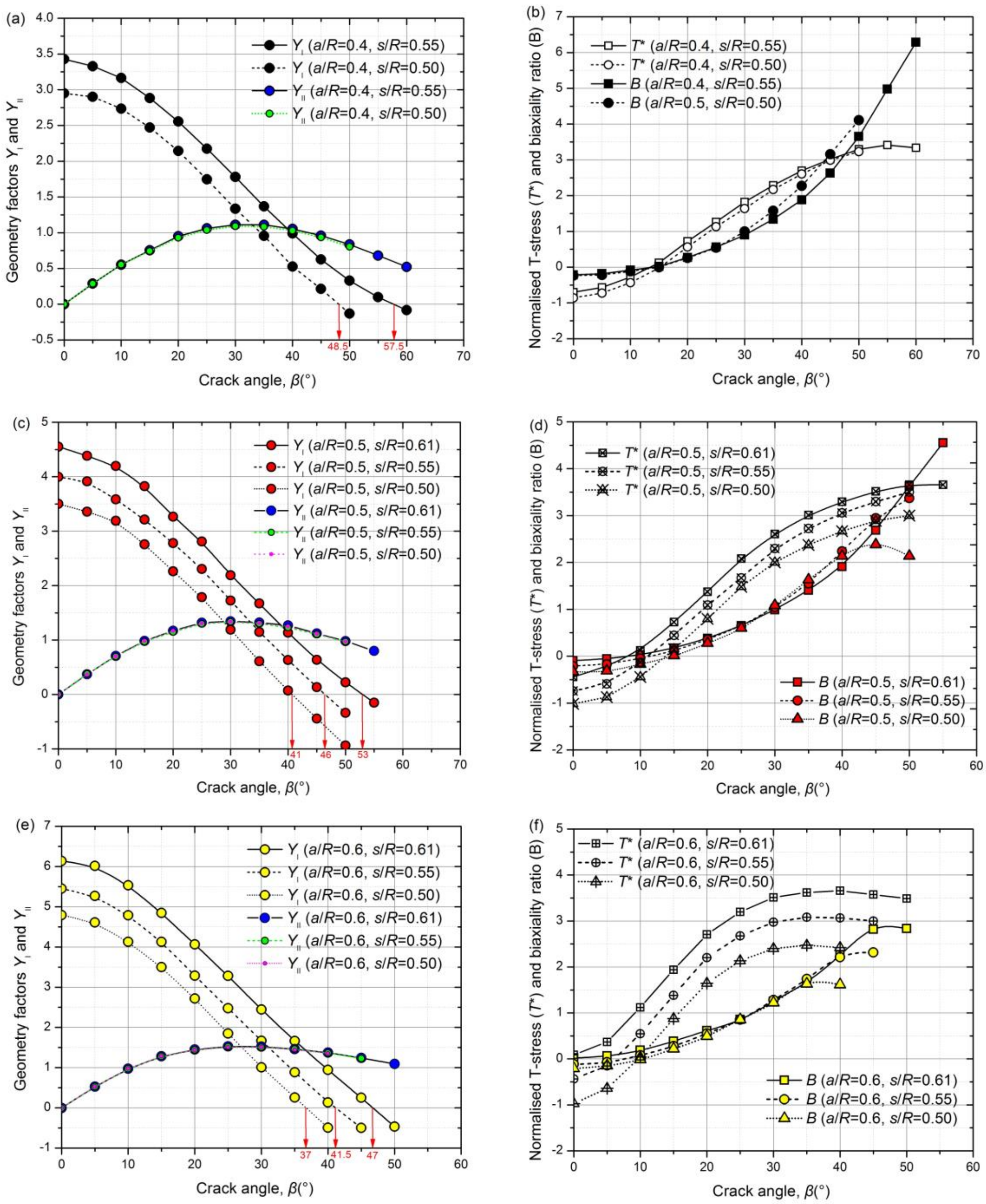
(a)
Geometry factors Y_I and Y_II
Crack angle, β(°)
Y_I (a/R=0.4, s/R=0.55)
Y_I (a/R=0.4, s/R=0.50)
Y_II (a/R=0.4, s/R=0.55)
Y_II (a/R=0.4, s/R=0.50)
48.5
57.5
(b)
Normalised T-stress (T*) and biaxiality ratio (B)
Crack angle, β(°)
T* (a/R=0.4, s/R=0.55)
T* (a/R=0.4, s/R=0.50)
B (a/R=0.4, s/R=0.55)
B (a/R=0.5, s/R=0.50)
(c)
Geometry factors Y_I and Y_II
Crack angle, β(°)
Y_I (a/R=0.5, s/R=0.61)
Y_I (a/R=0.5, s/R=0.55)
Y_I (a/R=0.5, s/R=0.50)
Y_II (a/R=0.5, s/R=0.61)
Y_II (a/R=0.5, s/R=0.55)
Y_II (a/R=0.5, s/R=0.50)
41
46
53
(d)
Normalised T-stress (T*) and biaxiality ratio (B)
Crack angle, β(°)
T* (a/R=0.5, s/R=0.61)
T* (a/R=0.5, s/R=0.55)
T* (a/R=0.5, s/R=0.50)
B (a/R=0.5, s/R=0.61)
B (a/R=0.5, s/R=0.55)
B (a/R=0.5, s/R=0.50)
(e)
Geometry factors Y_I and Y_II
Crack angle, β(°)
Y_I (a/R=0.6, s/R=0.61)
Y_I (a/R=0.6, s/R=0.55)
Y_I (a/R=0.6, s/R=0.50)
Y_II (a/R=0.6, s/R=0.61)
Y_II (a/R=0.6, s/R=0.55)
Y_II (a/R=0.6, s/R=0.50)
37
41.5
47
(f)
Normalised T-stress (T*) and biaxiality ratio (B)
Crack angle, β(°)
T* (a/R=0.6, s/R=0.61)
T* (a/R=0.6, s/R=0.55)
T* (a/R=0.6, s/R=0.50)
B (a/R=0.6, s/R=0.61)
B (a/R=0.6, s/R=0.55)
B (a/R=0.6, s/R=0.50)

Fig 3

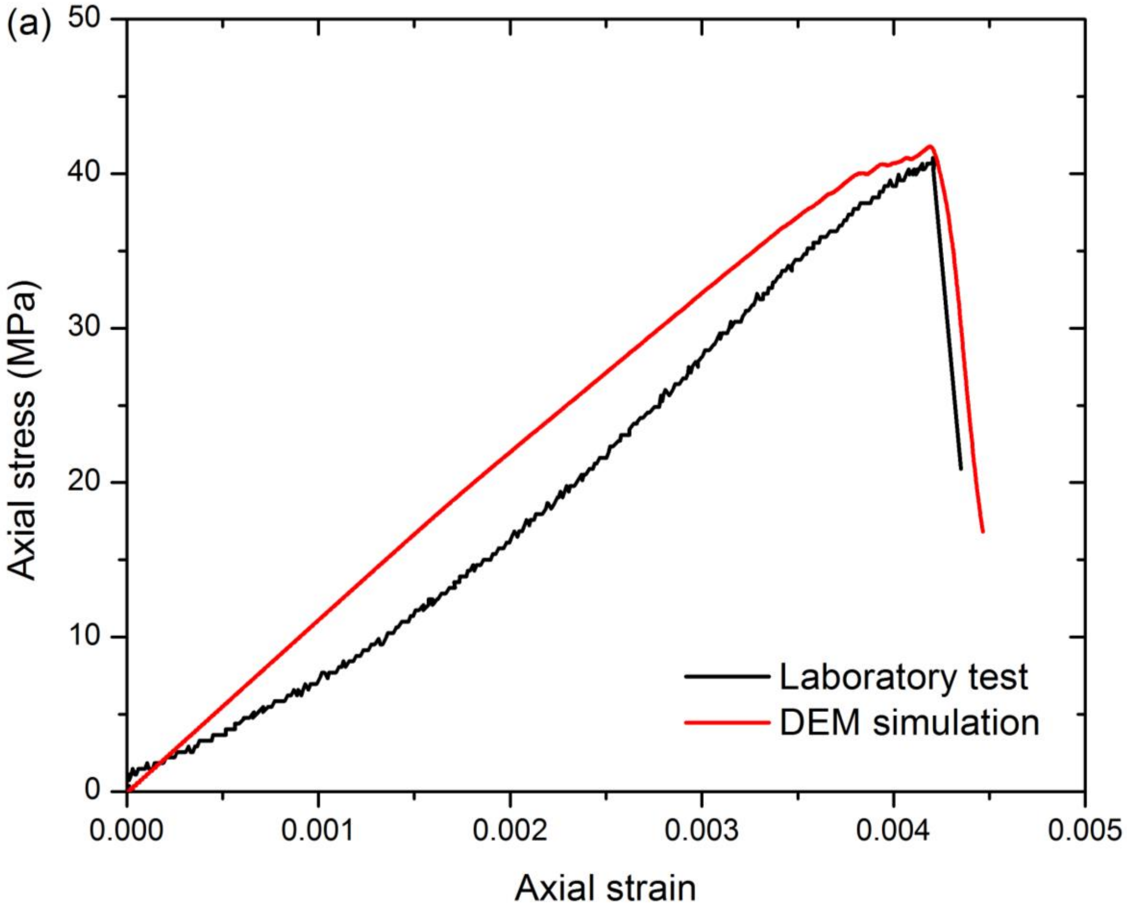

Fig 4

ACCEPTED

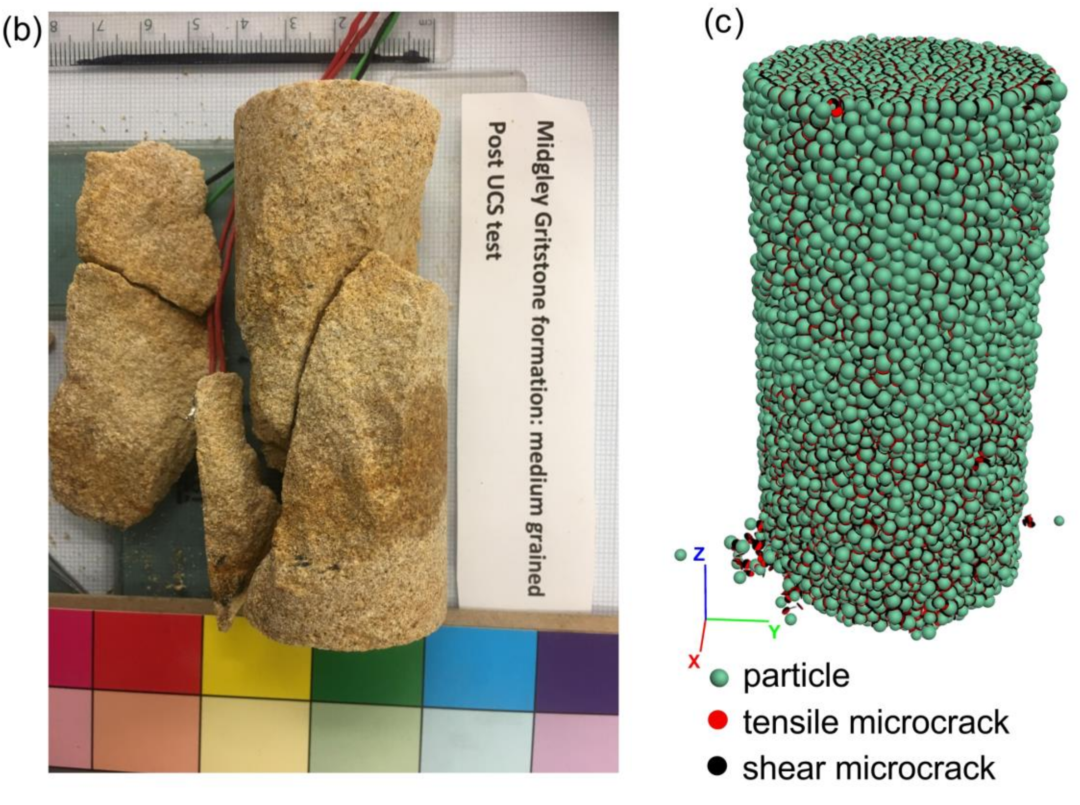

Fig 4 Continued

ACCEPTED MAN

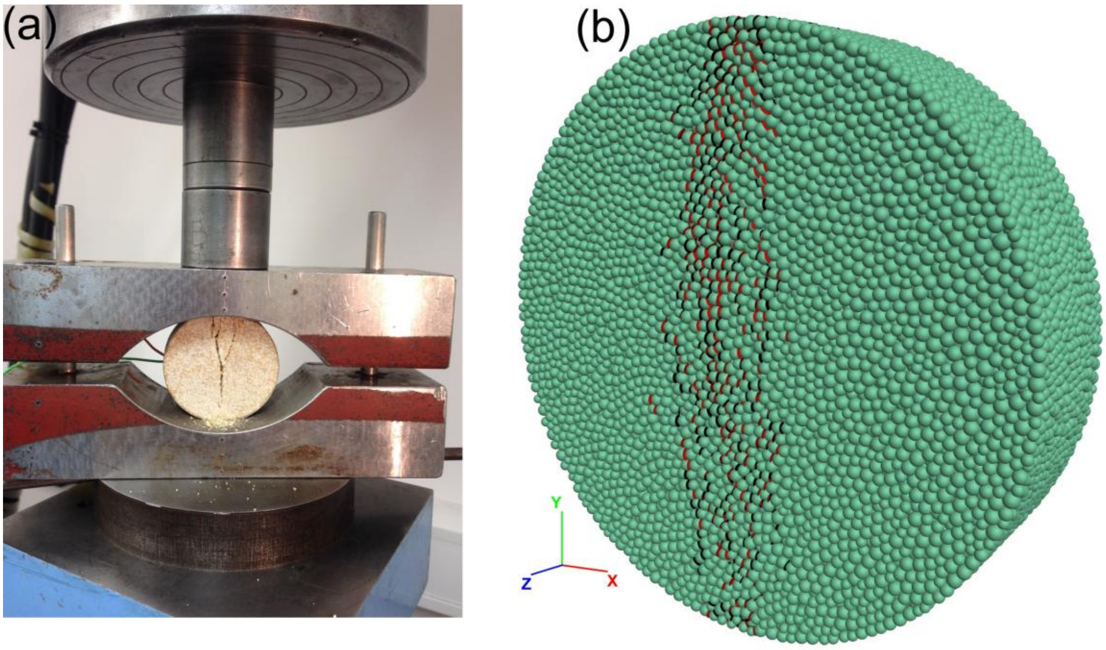

Fig 5

ACCEPTED MANUSC

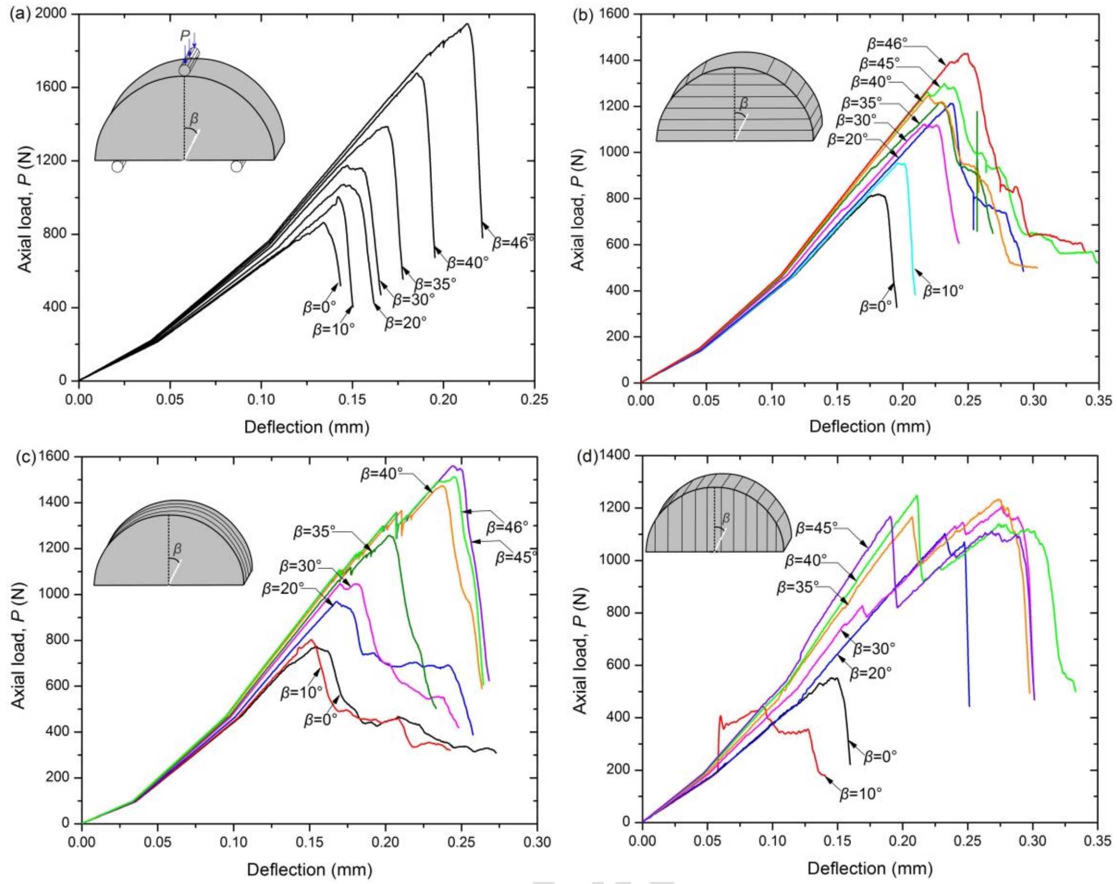

Fig 6

ACCEPTED MANUSCRIPT

943

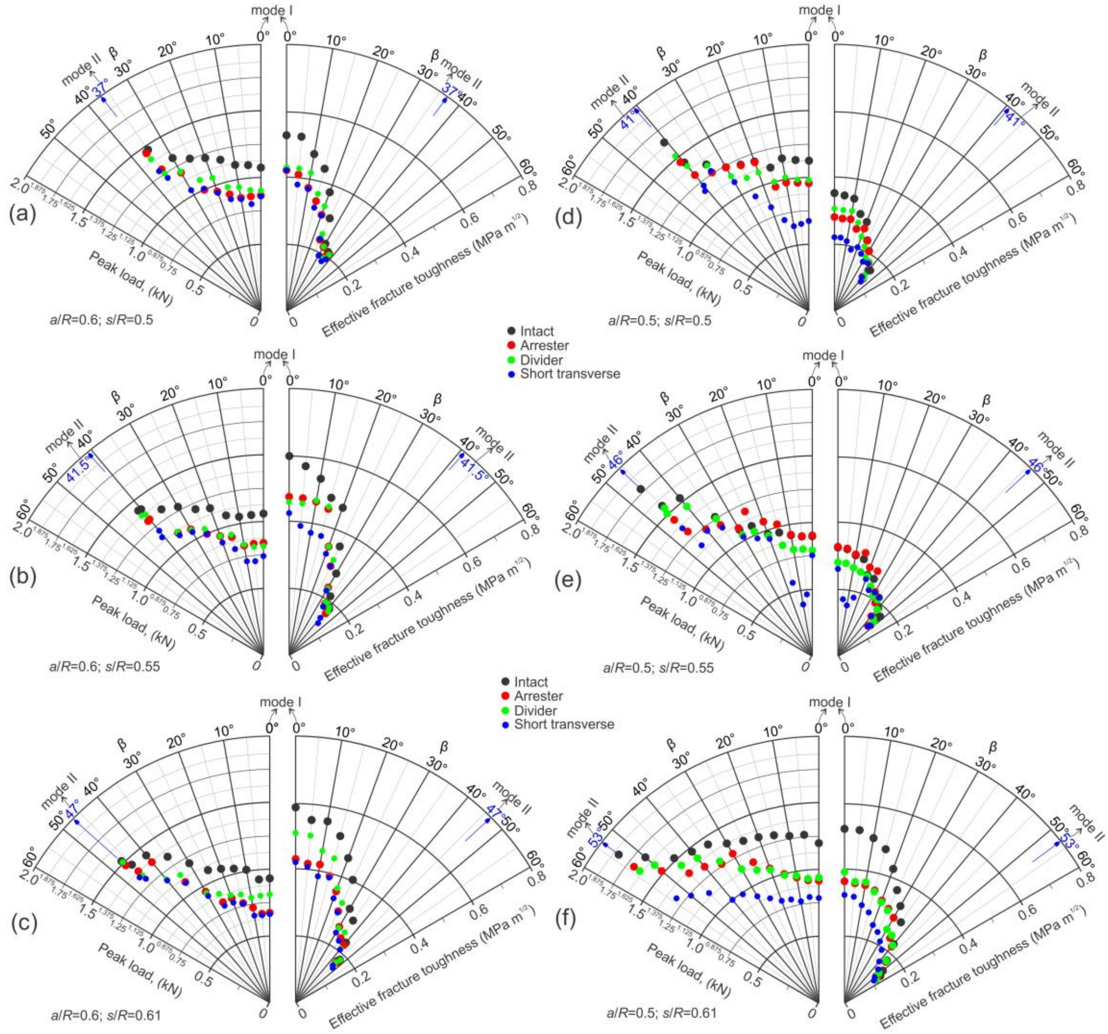

944 **Fig 7**

ACCEPTED

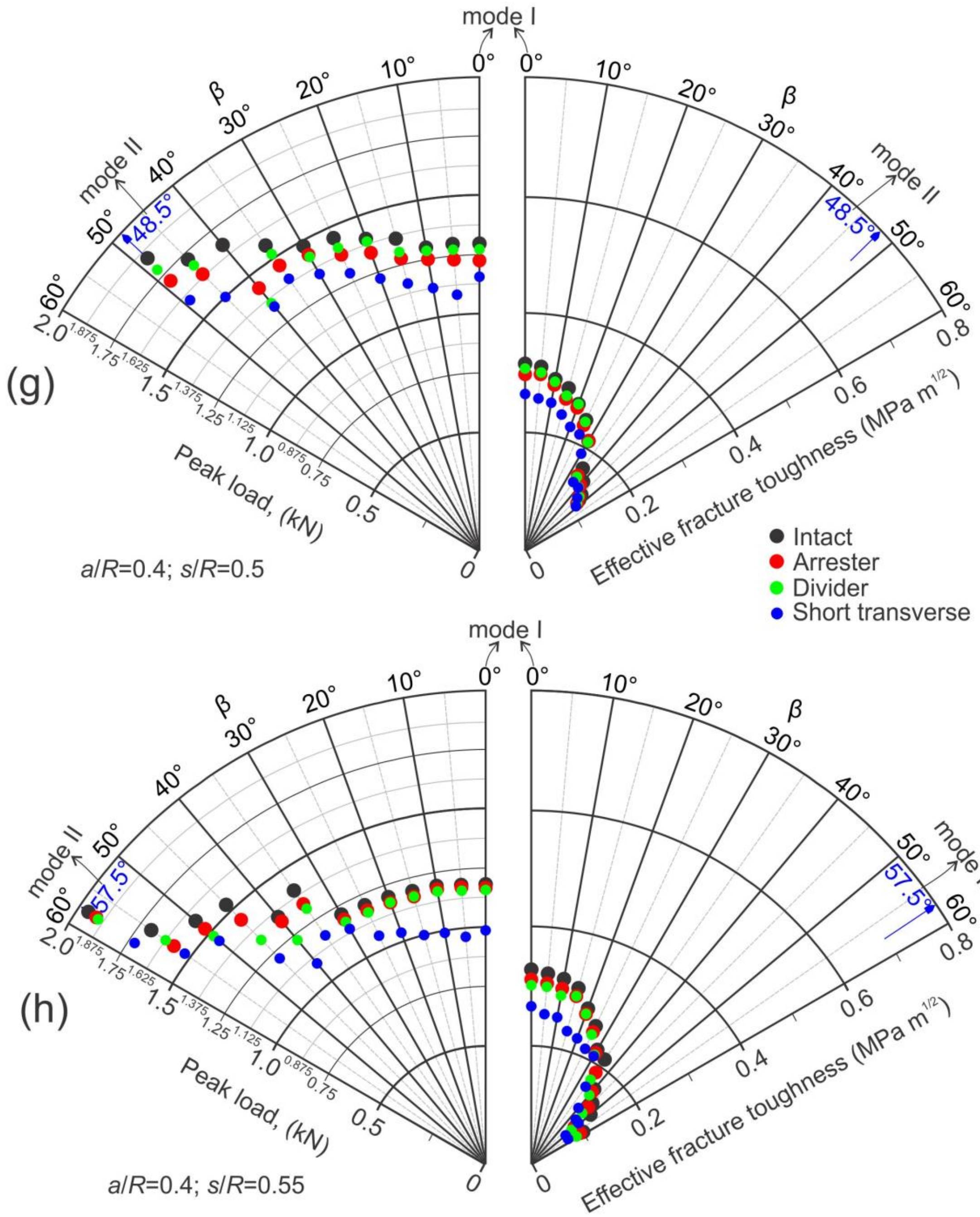

Fig 7 Continued

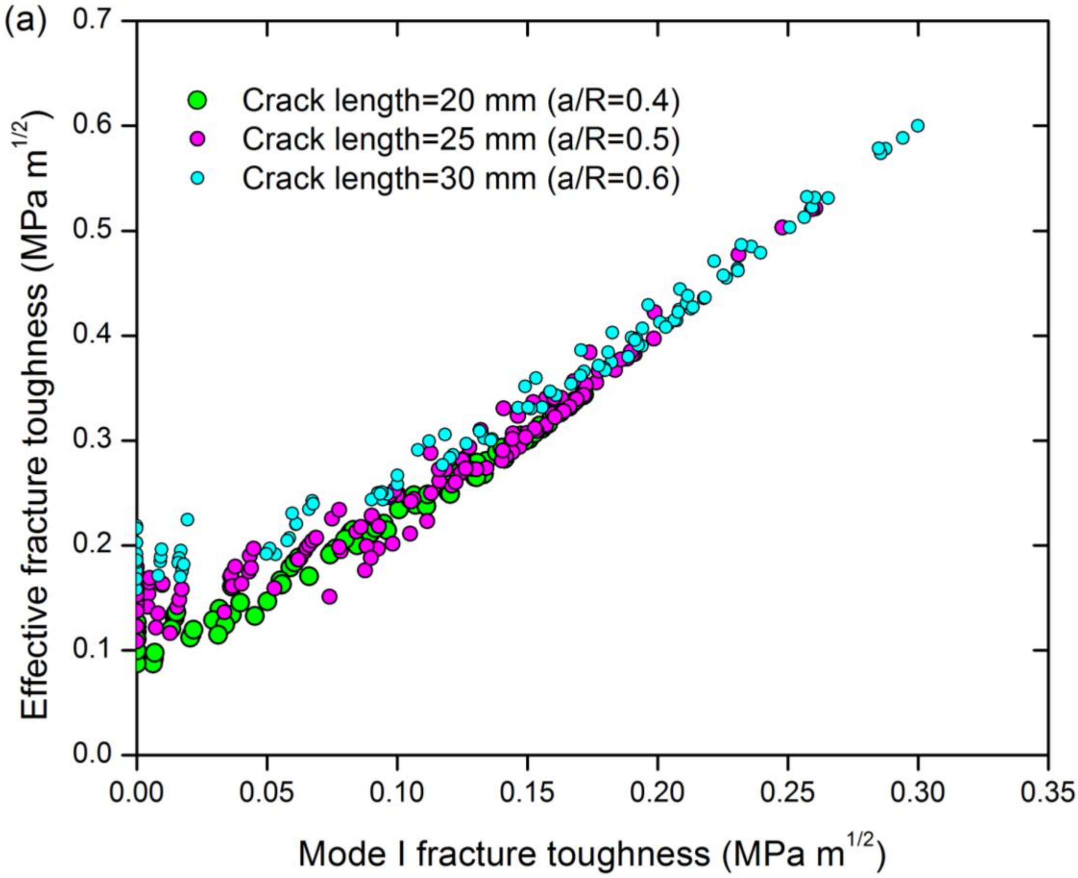

Fig 8a

ACCEPTED M

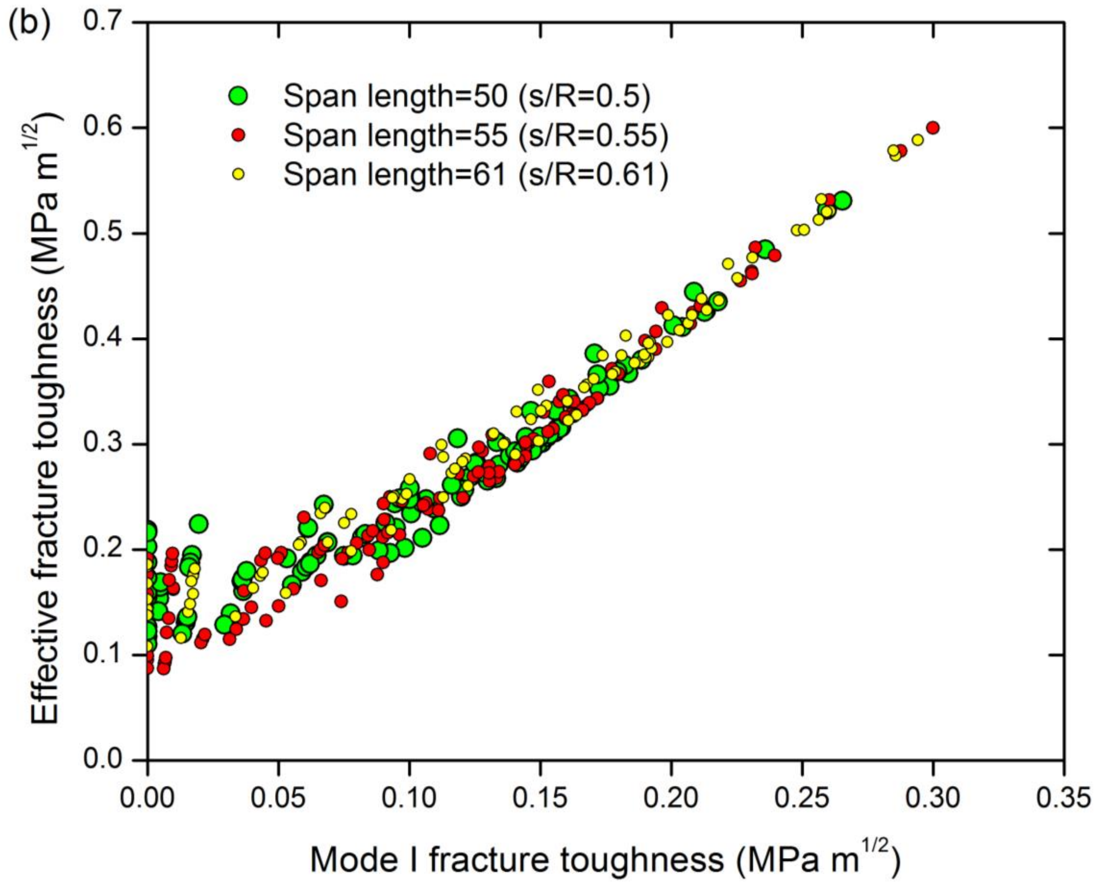

957

958 **Fig 8b**

ACCEPTED MA

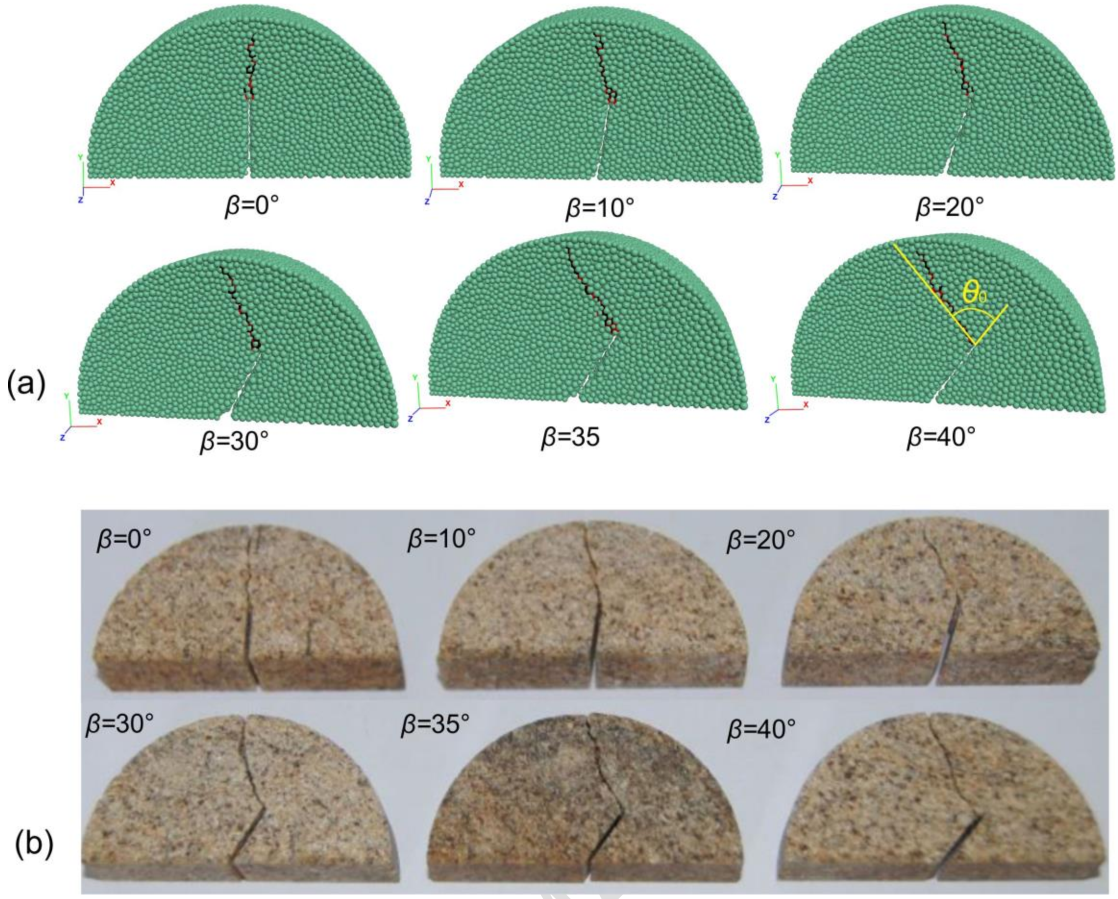

Fig 9

ACCEPTED MA

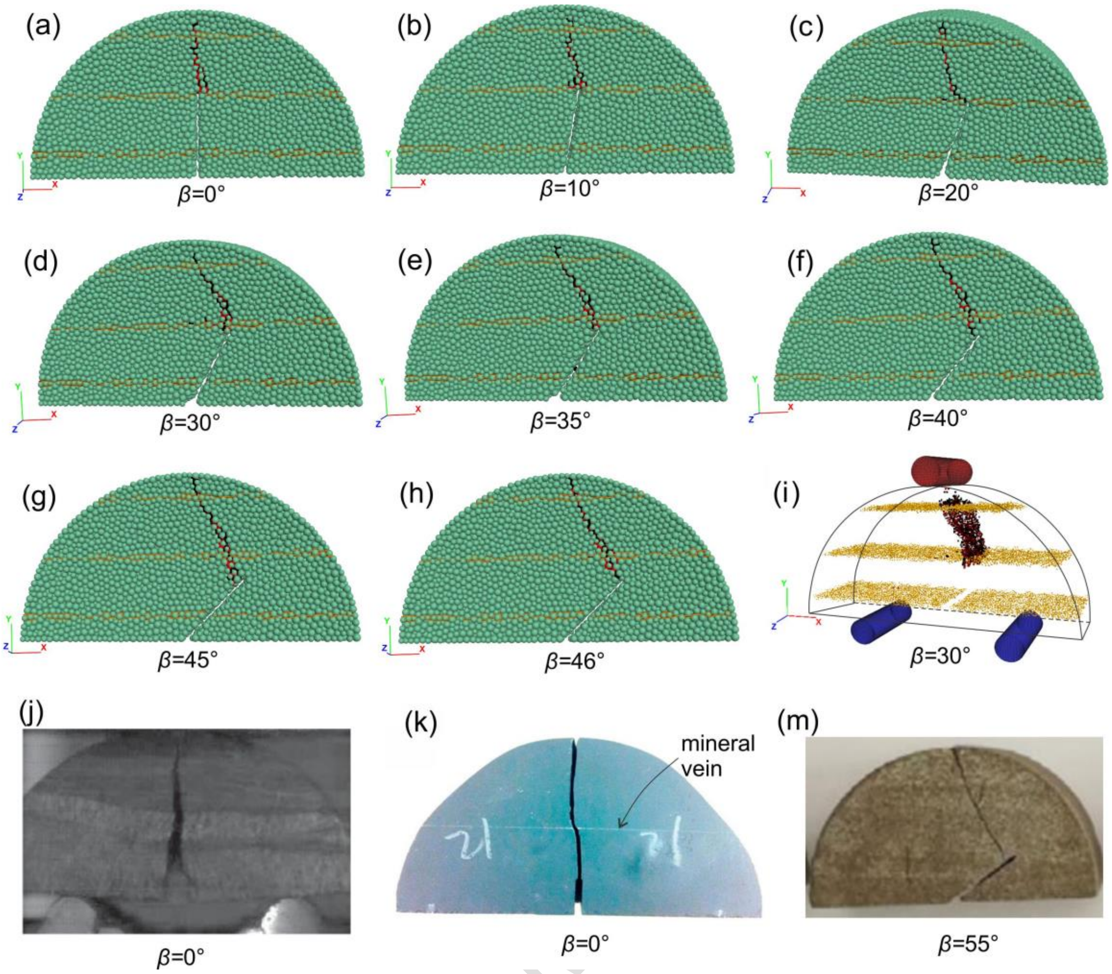

Fig 10

ACCEPTED

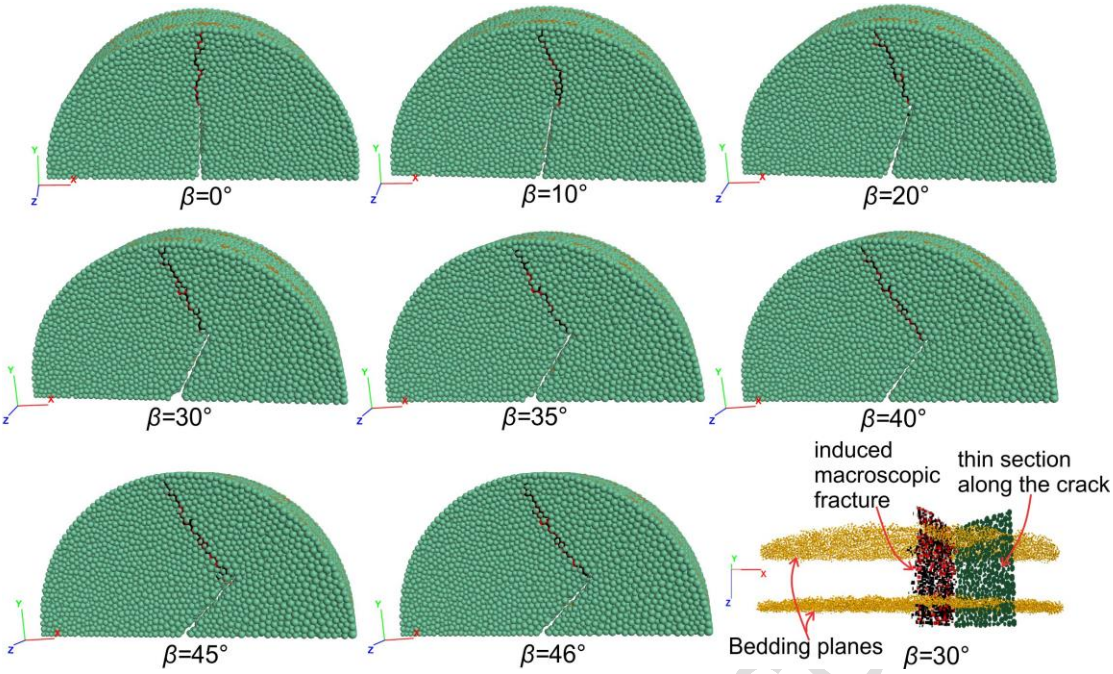

Fig 11

ACCEPTED MANUSCRIPT

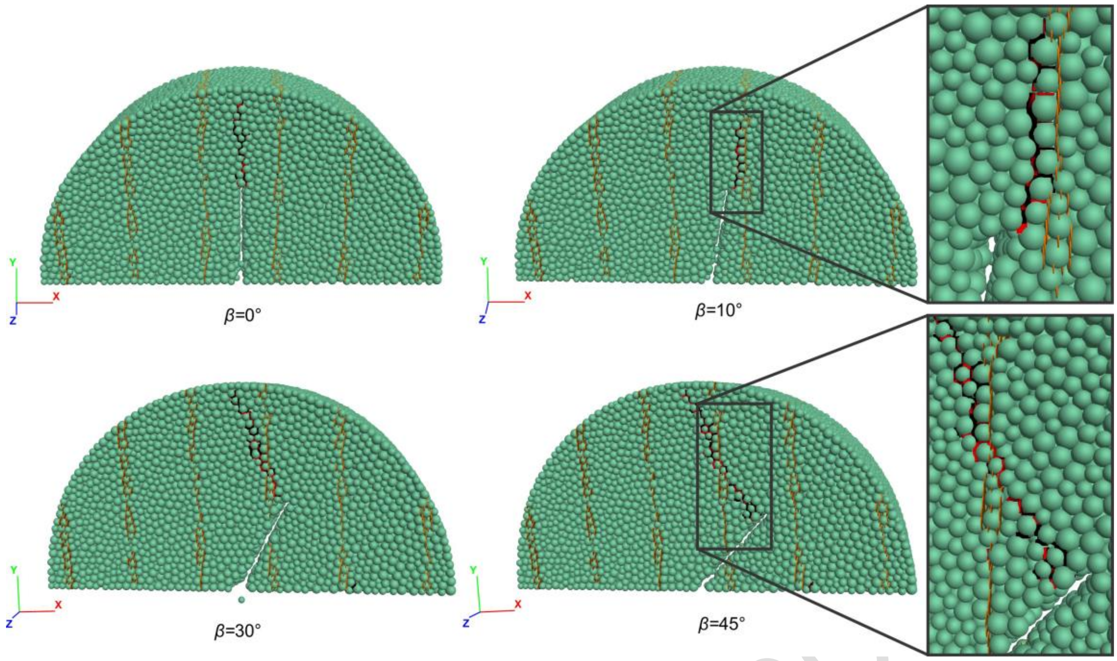

Fig 12

ACCEPTED MANUSC

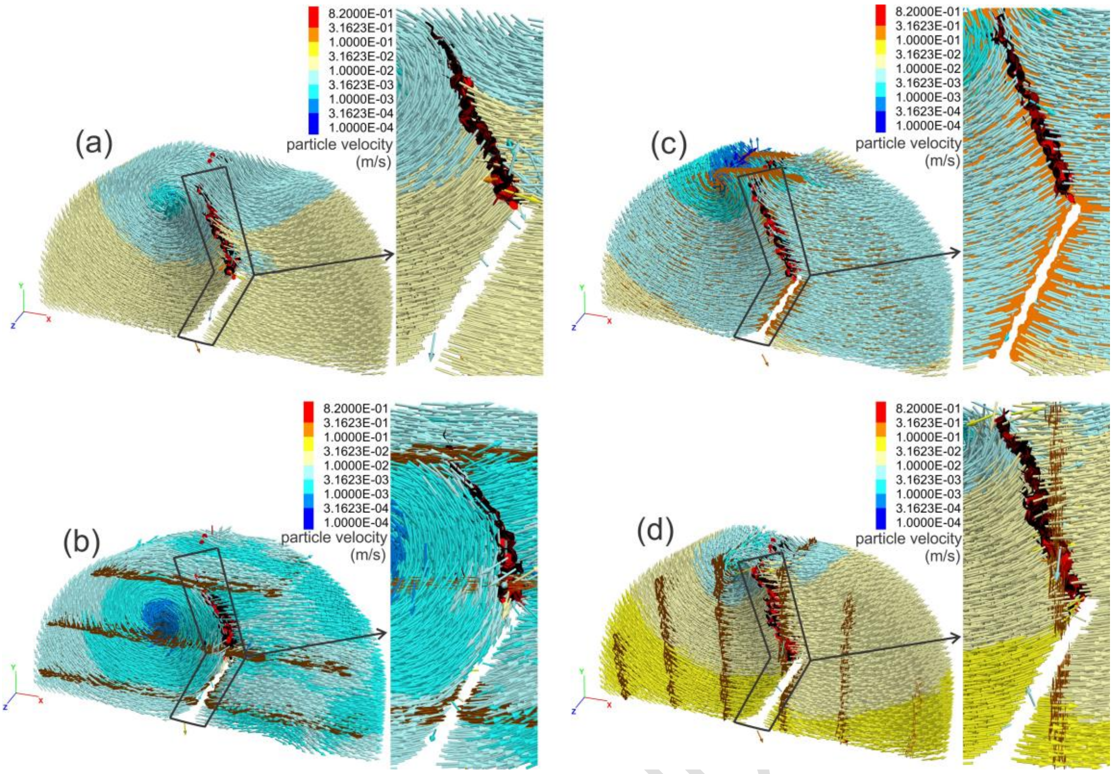

Fig 13

ACCEPTED MANU

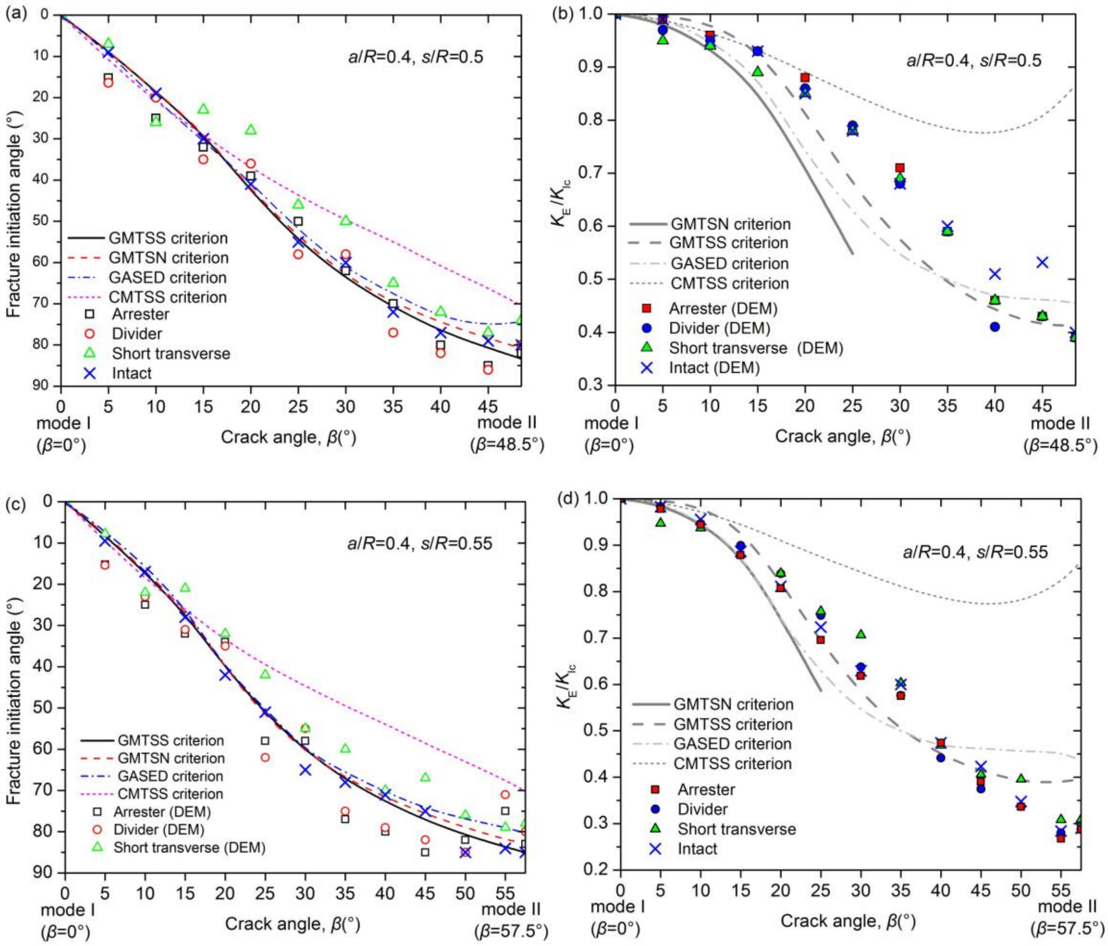
(a)
a/R=0.4, s/R=0.5
Fracture initiation angle (°)
GMTSS criterion
GMTSN criterion
GASED criterion
CMTSS criterion
Arrester
Divider
Short transverse
Intact
mode I
(β=0°)
Crack angle, β(°)
mode II
(β=48.5°)
(b)
a/R=0.4, s/R=0.5
K_E/K_Ic
GMTSN criterion
GMTSS criterion
GASED criterion
CMTSS criterion
Arrester (DEM)
Divider (DEM)
Short transverse (DEM)
Intact (DEM)
mode I
(β=0°)
Crack angle, β(°)
mode II
(β=48.5°)
(c)
a/R=0.4, s/R=0.55
Fracture initiation angle (°)
GMTSS criterion
GMTSN criterion
GASED criterion
CMTSS criterion
Arrester (DEM)
Divider (DEM)
Short transverse (DEM)
mode I
(β=0°)
Crack angle, β(°)
mode II
(β=57.5°)
(d)
a/R=0.4, s/R=0.55
K_E/K_Ic
GMTSN criterion
GMTSS criterion
GASED criterion
CMTSS criterion
Arrester
Divider
Short transverse
Intact
mode I
(β=0°)
Crack angle, β(°)
mode II
(β=57.5°)

Fig 14

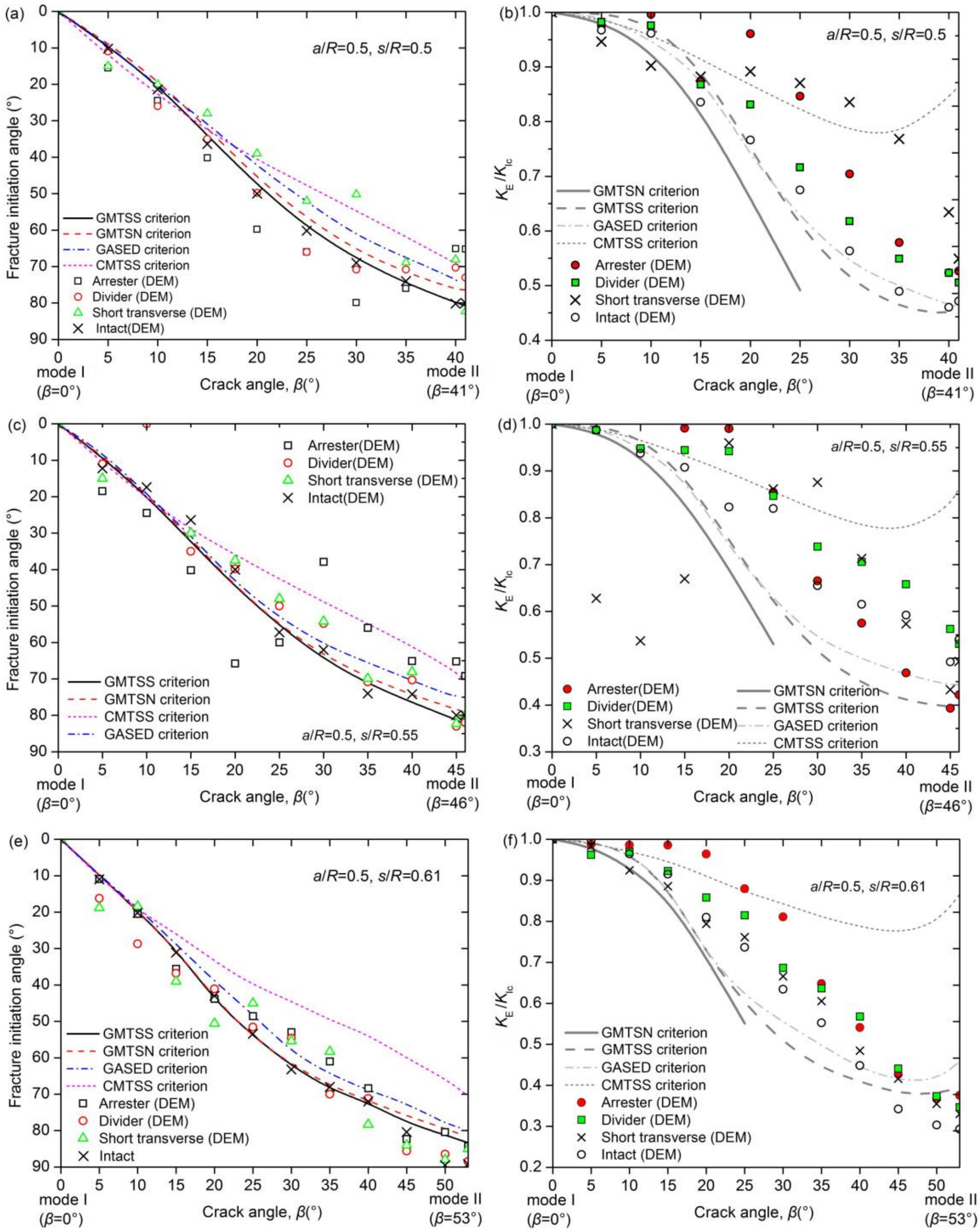
(a)
a/R=0.5, s/R=0.5
Fracture initiation angle (°)
GMTSS criterion
GMTSN criterion
GASED criterion
CMTSS criterion
Arrester (DEM)
Divider (DEM)
Short transverse (DEM)
Intact(DEM)
mode I (β=0°)
Crack angle, β(°)
mode II (β=41°)
(b)
a/R=0.5, s/R=0.5
K_E /K_Ic
GMTSN criterion
GMTSS criterion
GASED criterion
CMTSS criterion
Arrester (DEM)
Divider (DEM)
Short transverse (DEM)
Intact (DEM)
mode I (β=0°)
Crack angle, β(°)
mode II (β=41°)
(c)
Arrester(DEM)
Divider(DEM)
Short transverse (DEM)
Intact(DEM)
Fracture initiation angle (°)
GMTSS criterion
GMTSN criterion
CMTSS criterion
GASED criterion
a/R=0.5, s/R=0.55
mode I (β=0°)
Crack angle, β(°)
mode II (β=46°)
(d)
a/R=0.5, s/R=0.55
K_E /K_Ic
Arrester(DEM)
Divider(DEM)
Short transverse (DEM)
Intact(DEM)
GMTSN criterion
GMTSS criterion
GASED criterion
CMTSS criterion
mode I (β=0°)
Crack angle, β(°)
mode II (β=46°)
(e)
a/R=0.5, s/R=0.61
Fracture initiation angle (°)
GMTSS criterion
GMTSN criterion
GASED criterion
CMTSS criterion
Arrester (DEM)
Divider (DEM)
Short transverse (DEM)
Intact
mode I (β=0°)
Crack angle, β(°)
mode II (β=53°)
(f)
a/R=0.5, s/R=0.61
K_E /K_Ic
GMTSN criterion
GMTSS criterion
GASED criterion
CMTSS criterion
Arrester (DEM)
Divider (DEM)
Short transverse (DEM)
Intact (DEM)
mode I (β=0°)
Crack angle, β(°)
mode II (β=53°)

Fig 15

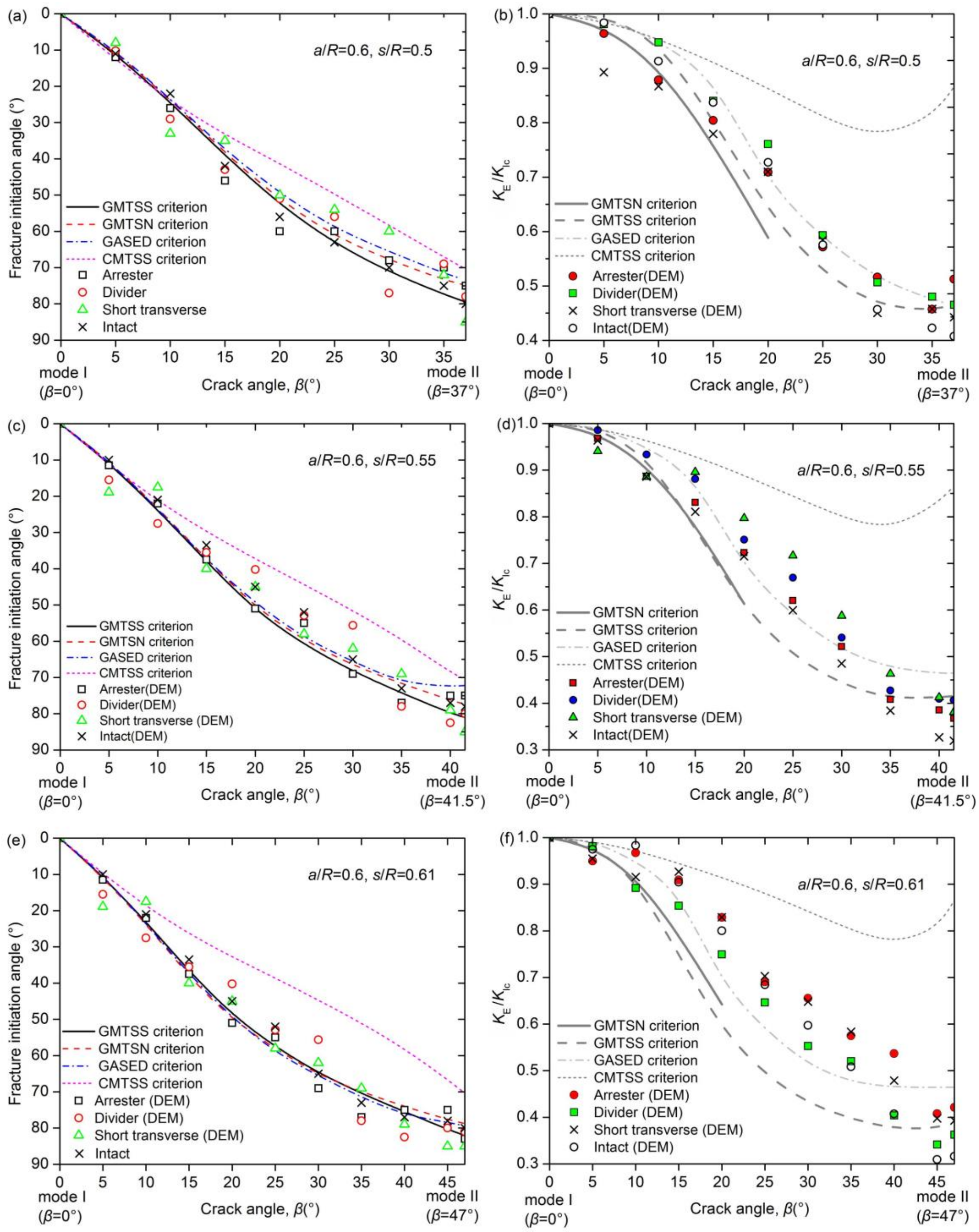
(a)
a/R=0.6, s/R=0.5
Fracture initiation angle (°)
GMTSS criterion
GMTSN criterion
GASED criterion
CMTSS criterion
Arrester
Divider
Short transverse
Intact
mode I (β=0°)
Crack angle, β(°)
mode II (β=37°)
(b)
a/R=0.6, s/R=0.5
KE /KIc
GMTSN criterion
GMTSS criterion
GASED criterion
CMTSS criterion
Arrester(DEM)
Divider(DEM)
Short transverse (DEM)
Intact(DEM)
mode I (β=0°)
Crack angle, β(°)
mode II (β=37°)
(c)
a/R=0.6, s/R=0.55
Fracture initiation angle (°)
GMTSS criterion
GMTSN criterion
GASED criterion
CMTSS criterion
Arrester(DEM)
Divider(DEM)
Short transverse (DEM)
Intact(DEM)
mode I (β=0°)
Crack angle, β(°)
mode II (β=41.5°)
(d)
a/R=0.6, s/R=0.55
KE /KIc
GMTSN criterion
GMTSS criterion
GASED criterion
CMTSS criterion
Arrester(DEM)
Divider(DEM)
Short transverse (DEM)
Intact(DEM)
mode I (β=0°)
Crack angle, β(°)
mode II (β=41.5°)
(e)
a/R=0.6, s/R=0.61
Fracture initiation angle (°)
GMTSS criterion
GMTSN criterion
GASED criterion
CMTSS criterion
Arrester (DEM)
Divider (DEM)
Short transverse (DEM)
Intact
mode I (β=0°)
Crack angle, β(°)
mode II (β=47°)
(f)
a/R=0.6, s/R=0.61
KE /KIc
GMTSN criterion
GMTSS criterion
GASED criterion
CMTSS criterion
Arrester (DEM)
Divider (DEM)
Short transverse (DEM)
Intact (DEM)
mode I (β=0°)
Crack angle, β(°)
mode II (β=47°)

Fig 16

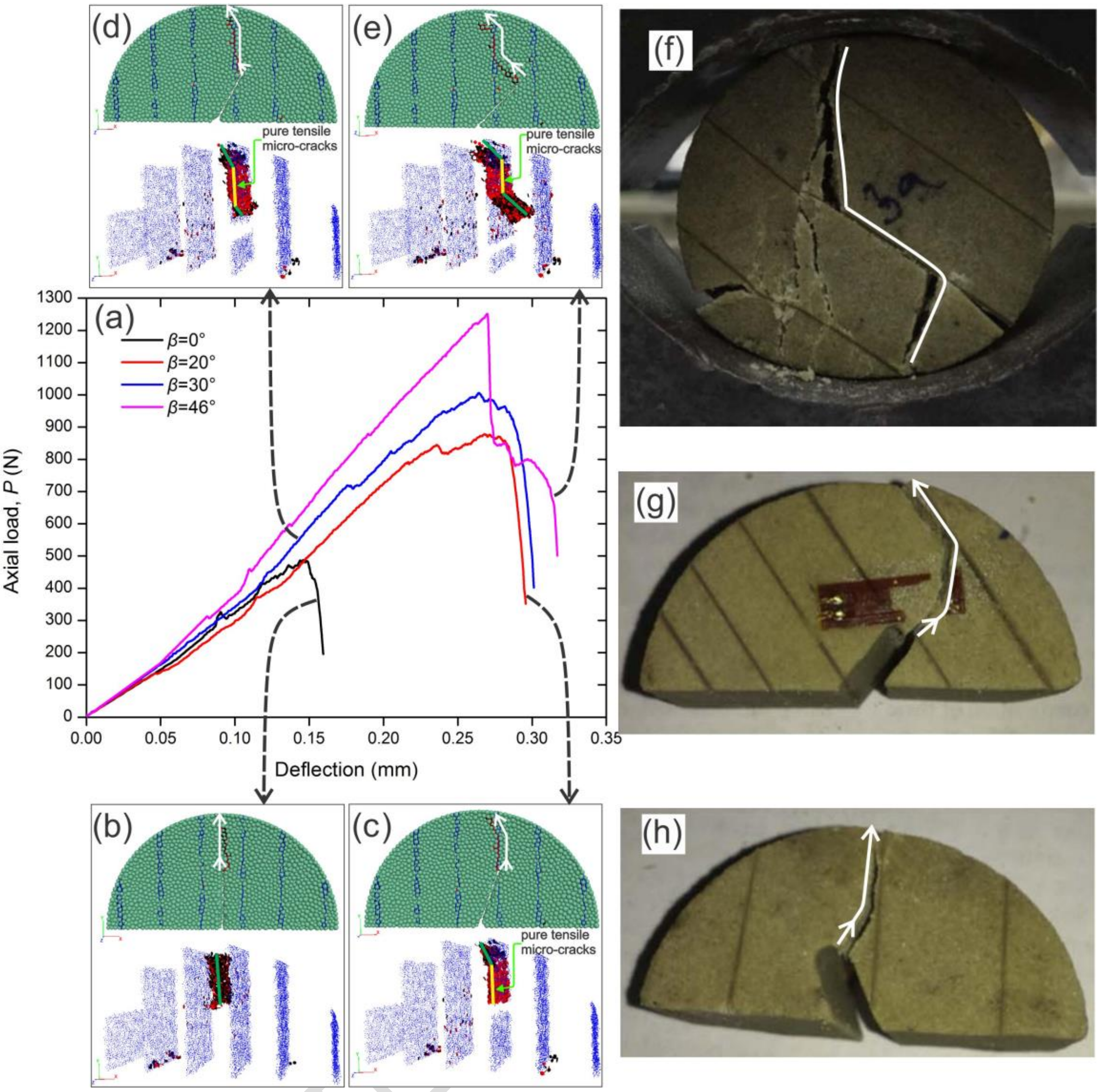

1003

1004 **Fig 17**

1005

1006

ACCEPTED